UNIVERSITY OF CALIFORNIA SAN DIEGO

Spin-dependent Wave Propagation in Waveguides, Metasurfaces and 3D Photonic Crystals

A dissertation submitted in partial satisfaction of the
requirements for the degree
Doctor of Philosophy

in

Electrical Engineering (Photonics)

by

Sara Kandil

Committee in charge:

Professor Daniel Sievenpiper, Chair
Professor Prabhakar Bandaru
Professor Leonid Butov
Professor Yu-Hwa Lo
Professor George Papen

2022

The dissertation of Sara Kandil is approved, and it is acceptable in quality and form for publication on microfilm and electronically.

University of California San Diego

2022

DEDICATION

To my Mom and Sister, it wouldn't have been without you.

EPIGRAPH

Strange about learning; the farther I go the more I see that I never knew even existed. A short while ago I foolishly thought I could learn everything - all the knowledge in the world. Now I hope only to be able to know of its existence, and to understand one grain of it. Is there time?

—Daniel Keyes

TABLE OF CONTENTS

LIST OF FIGURES

LIST OF TABLES

ACKNOWLEDGEMENTS

I first arrived to the U.S. (and to UCSD) to start my PhD on September 15th, 2017. Now, five years have passed and my PhD journey has come to an end. I am extremely grateful for this journey and how it has changed me personally and academically. And what is a journey without people? The most important part of my journey is the amazing people I was fortunate to meet and who had great influence on shaping my research personality, identity and making my journey richer and more fruitful. And for that, I owe them a debt of gratitude.

I would like to thank my supervisor, Professor Daniel Sievenpiper for his continuous support. I feel extremely lucky to have worked under Prof. Dan's supervision during my PhD. His intuition and creativity have always amazed me. He gives his students the confidence to think out of the box and come up with new ideas. I really appreciate how this has greatly shaped my research personality.

I would like to thank my committee members, Professor Prabhakar Bandaru, Professor Yu-Hwa Lo, Professor George Papen, and Professor Leonid Butov. Thank you for your time and your feedback on my work. I have taken classes with each one of you and have been influenced by your breadth of knowledge and passion to the areas of photonics, solid-state physics and material science. I have collaborated with Prof. Prabhakar Bandaru on the Hydrogen ion project and have learned a lot from our discussions and his guidance.

To all the members of the Applied Electromagnetics Lab, thanks for all the great times, cooking, hiking and endless chats and laughs. You have made my time in the lab so fun and the hard times much easier. To Dia'aaldin Bisharat, thank you for mentoring me on the chiral metasurfaces project and for always being supportive.

Thanks to Yun Zhou for her help in getting me started on the Screw Dislocation project and for providing me with her code to use. Thanks for all the night walks back home and chats about everything. Robert Davis, my desk neighbour and the one who always motivates me. Thank you for being a great friend and always the first person to offer to help out. Thank you for your

24/7 maintenance support on the cluster and for the endless chats we had in the lab about science, books and philosophy.

Shreya Singh and Jiyeon Lee, thank you both for welcoming me to the lab when I first joined and taking me to so many places. You made my transition from Egypt coming here and to the lab much easier by your kindness and generosity. Erda and Xiaozhen, I enjoyed seeing your cat jumping between your two screens in the zoom meetings. Thank you both for always offering to help when I am working on experiments in the lab. Thank you Erda for teaching us how to use blender and for helping me making Fig. 3.1.

Thanks to Matthew Davis for being extremely supportive and motivating me with his kind words whenever I bump into him in the lab. Thanks to Kyle for all the fun stories about his fish project. Xianghong, Zhixia 1 and Zhixia 2, I have enjoyed your company and learned from you even for a short time.

Big thanks to the Egyptian community here who have showered me with their love and care throughout the five years I spent here. I have not met anyone as kind as they are and they have taught me so much on the personal level. They brought Egypt to me here and made my stay away from my family less harder. Also, thanks for all the delicious Egyptian food.

I would like to thank my friends in Egypt who kept my company and supported me even though we were 7600 miles away and 10 hours time different. Thanks to Rania, Esraa, Mai, Shereen, and Hoda.

Last, but actually the most important part: thanks to my family, specifically, my mom and sister. You have been my support system through it all and I literally wouldn't have been able to do anything without you by my side. I owe you everything and I feel extremely lucky to have you in my life.

The material in this dissertation is based on the following papers which are either published or in preparation for publication.

Chapter 2 is based on *C-shaped Chiral Waveguide for Spin-dependent Unidirectional*

Propagation by S. Kandil, and D. Sievenpiper, *Applied Physics Letters*. The dissertation author was the primary author of this material.

Chapter 3 is based on *Engineering Equifrequency Contours of Metasurfaces for Self-Collimated Surface Wave Steering* by S. Kandil, D. Bisharat and D. Sievenpiper, *In preparation*. The dissertation author was the primary author of this material.

Chapter 4 is based on *Chiral surface wave propagation with anomalous spin-momentum locking* by S. Kandil, D. Bisharat and D. Sievenpiper, *ACS Photonics*. The dissertation author was the primary author of this material.

Chapter 5 is based on *Screw Dislocation in Diamond Photonic Crystal for Spin- dependent Propagation* by S. Kandil, Y. Zhou, P. R. Bandaru and D. Sievenpiper, *In preparation*. The dissertation author was the primary author of this material.

All material is used with permission by the co-authors.

VITA

2014	B. S. in Electrical Engineering *with honors*, Cairo University, Egypt
2017	M. S. in Electrical Engineering, specialization in electromagnetics, Cairo University, Egypt
2022	Ph. D. in Electrical Engineering (Photonics), University of California San Diego

PUBLICATIONS

Sara M. Kandil, Yun Zhou, Prabhakar Bandaru, D. Sievenpiper, "*Screw dislocation in 3D Diamond photonic crystal for spin-dependent wave propagation*," *In preparation*.

Sara M. Kandil, D. Bisharat, D. Sievenpiper, "*C-shaped metasurface for polarization-based surface wave steering*," *In preparation*.

Sara M. Kandil, Anna Alexander, Kevin Jensen, Prabhakar Bandaru, Nathan Moody, Daniel F. Sievenpiper, *"Photo-controlled solid-state negative hydrogen ion source*," *In preparation*.

Sara M. Kandil, Dia'aaldin J. Bisharat, Daniel F. Sievenpiper, "*Chiral Surface Wave propagation with Anomalous Spin-momentum Locking*", ACS Photonics (2022).

Shreya Singh, Robert J. Davis, Dia'aaldin J. Bisharat, Jiyeon Lee, **Sara M. Kandil**, Erda Wen, Xiaozhen Yang, Yun Zhou, Prabhakar R.Bandaru and Daniel F. Sievenpiper, "*Advances in metasurfaces: topology, chirality, patterning, and time modulation*", IEEE Antennas and Propagation Magazine (2021).

Sara M. Kandil, D. Sievenpiper, "*C-shaped Chiral Waveguide for Spin-dependent Unidirectional Propagation*," Applied Physics Letters (2021).

Sara M. Kandil, Islam A. Eshrah, Inas S. El Babli, and Ashraf H. Badawi, "Plasmon hybridization in split ring nanosandwich for refractive index sensing," in Optics Express, December 2016.

Mai O. Sallam, **Sara M. Kandil**, Vladimir Volski, Guy A. E. Vandenbosch, and Ezzeldin A. Soliman, "CPW-fed flexible bow-tie slot antenna for WLAN/WiMax systems" in IEEE Transactions on Antennas and Propagation, June 2017.

CONFERENCES and TALKS

Sara M. Kandil, D. Bisharat and D. Sievenpiper, "*Metasurfaces for spin-control of surface waves*," SPIE Photonics West 2022, San Francisco.

Sara M. Kandil, Anna Alexander, Kevin Jensen, Prabhakar Bandaru, Daniel F. Sievenpiper, Nathan A. Moody, "*Photo-controlled solid-state negative hydrogen ion source*," SPIE Photonics West 2022, San Francisco

Sara M. Kandil and D. Sievenpiper, "*Chiral Waveguides for Spin-dependent propagation*," MetaNano 2021.

Sara M. Kandil, "*Metasurfaces for spin-control of surface waves*," Rising Stars in EECS workshop.

Sara M. Kandil, D. Bisharat, D. Sievenpiper, "*Spin-momentum Locking of Chiral Surface waves*," Metamaterials, October 2020

Sara M. Kandil, D. Bisharat, D. Sievenpiper, "*C-shaped metasurface for polarization-based surface wave steering*," SPIE Optics and Photonics: Metamaterials, Metadevices, and Metasystems, Aug 24-28, 2020

Sara M. Kandil, "*Metasurfaces for Chiral Surface Waves*," Lab Expo Graduate Showcase, Feb 2020.

D. Bisharat, **S. Kandil**, X, Kong, S. Singh, Z. Xu, D. Sievenpiper, "*Chiral and Topological Surface Waves and Line Waves on Metasurfaces*" Metamaterials 2019, Rome, Italy, September 16-21, 2019

Sara M. Kandil, D. Bisharat, D. Sievenpiper, "*L-shaped Metasurface for Chiral Surface Waves Propagation*", IEEE Antennas and Propagation Symposium, Atlanta, GA, July 7-12, 2019

Sara M. Kandil, Islam A. Eshrah, Inas S. El Babli, and Ashraf H. Badawi, "*Asymmetric split ring nanosandwich for refractive index sensing*," in the 11th European Conference for Antenna and Propagation (EuCAP), March 2017.

Sara M. Kandil, Inas S. El Babli, and Ashraf H. Badawi, "*Study of the gap influence on highly sensitive plasmonic nanosandwich for refractive index sensing*," European Conference for Antenna and Propagation (EuCAP), Davos, Switzerland, April 2016.

Sara M. Kandil, Tamer A. Ali, Sherif Sedky, and Ezzeldin A. Soliman, "*Highly sensitive mushroom-shaped gold-silica nano antenna array for refractive index sensing*" European Conference for Antenna and Propagation (EuCAP), Davos, Switzerland, April 2016.

Mai O. Sallam, **Sara M. Kandil**, Vladimir Volski, Guy A. E. Vandenbosch, and Ezzeldin A. Soliman, "*Flexible Bow-Tie Antenna for WLAN/Wi-Max Applications*" European Conference for Antenna and Propagation (EuCAP), Davos, Switzerland, April 2016.

Mai O. Sallam, **Sara M. Kandil**, Vladimir Volski, Guy A. E. Vandenbosch, and Ezzeldin A. Soliman, "*2.4/5 GHz WLAN crescent antenna on flexible substrate*" European Conference for Antenna and Propagation (EuCAP), Davos, Switzerland, April 2016.

ABSTRACT OF THE DISSERTATION

Spin-dependent Wave Propagation in Waveguides, Metasurfaces and 3D Photonic Crystals

by

Sara Kandil

Doctor of Philosophy in Electrical Engineering (Photonics)

University of California San Diego, 2022

Professor Daniel Sievenpiper, Chair

Photon spin has received great interest in the recent decades for many applications such as encoding quantum information and spin-filtering. However, very little is known about controlling the direction and properties of the spin. It was recently found that surface waves with evanescent tails possess an inherent in-plane transverse spin which is dependent on the propagation direction.

In this dissertation, we investigate different 1D, 2D and 3D designs that support strong spin-dependent propagation. Starting with a 1D C-shaped waveguide, we show that the spin-density can be enhanced through dipole-to-dipole coupling resulting in highly directional wave propagation. We then show spin-dependent wave splitting in 2D metasurface by engineering the equifrequency contours. We demonstrate the possibility of steering the surface wave along curved

paths. We also introduce a new type of surface wave called a chiral surface wave which has two transverse spins, an in-plane one that is inherent to any surface wave and an out-of-plane spin which is enforced by the design due to strong x-to-y coupling and broken rotational symmetry. We show that the two transverse spins are locked to the momentum providing a highly confined spin-dependent propagation. Similar chiral modes can be induced in 3D structures by introducing screw dislocation defect in a diamond photonic crystal.

Our study opens a new direction for enhancing and controlling the spin properties of electromagnetic waves through engineering the symmetry of shapes in 1D, 2D and 3D. This provides an additional degree of freedom to control the propagation direction as well as the transverse spin of electromagnetic waves.

Chapter 1

Introduction

1.1 Spin-Hall Effect and Spin-momentum Locking

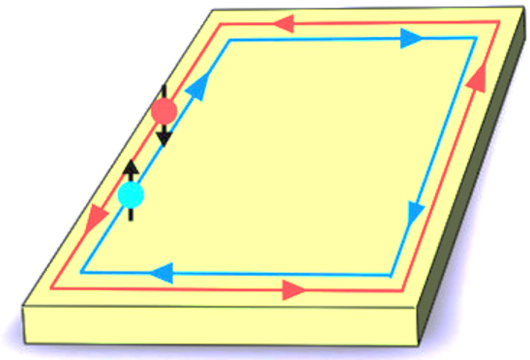

Figure 1.1: Spin Hall Effect in electronic systems (Source: [1]).

Spin is a universal property inherent to electrons and photons. Electron spin has been the origin of many intriguing phenomena such as Spin Hall Effect (SHE). SHE in electronic systems is characterized by the spin-dependent transport of electrons where electrons [2]. As shown in Fig. 1.1, a sample carrying electric current will have spin accumulation on its lateral surface where opposite spins propagate in opposite directions. This has opened the door for many applications in spintronics and quantum physics [3, 4]. It is also of great importance for

providing platforms that can carry information with high robustness against defects which led to the discovery of topological insulators [5–8].

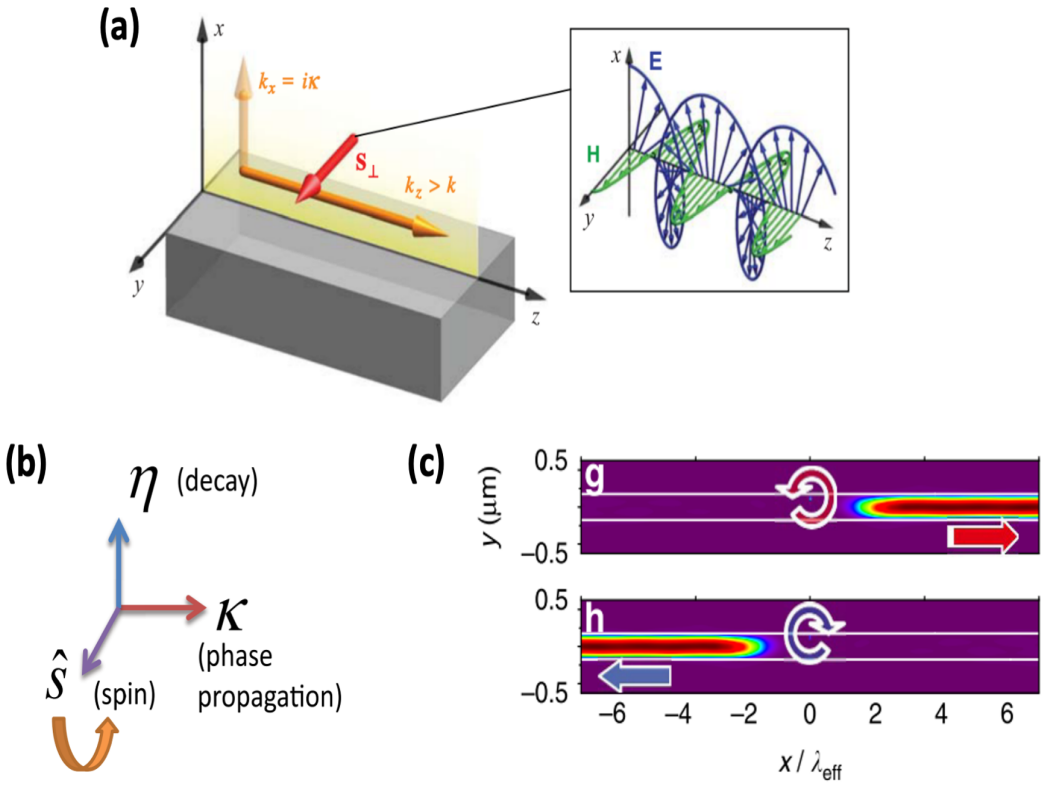

Figure 1.2: (a) Transverse spin for evanescent electromagnetic waves where spin represents E or H rotation (Source: [9]). (b) Schematic demonstrating spin-momentum locking formed of the right-hand triplet formed of Spin, decay constant and propagation constant (Source: [10]). (c) Demonstration of spin-dependent propagation where opposite handedness of CP wave propagate in opposite directions (Source: [11])

On the other hand, a photon's spin is associated with its polarization state, described as the handedness of its circular polarization (CP) where the spin vector is normal to the plane of the field rotation as illustrated in Fig. 1.2(a). Despite electrons and photons being fundamentally different particles, they reveal similar spin-related properties among which is the SHE. It was recently discovered that analogous to SHE in electrons, surface waves (SWs) with evanescent tails obtain an in-plane transverse spin (T-spin) that is locked to the propagation direction [9, 12, 13]. This is also known as spin-momentum locking which is defined as the right-hand triplet formed of the

decay constant, spin and propagation constant [10, 14] as depicted in Fig. 1.2(b). Spin-momentum locking results in a spin-dependent propagation for the electromagnetic waves where opposite CP handedness propagate in opposite directions as shown in Fig. 1.2(c).

1.2 Spin density of Surface waves

In this section, we will go through the formulations for evaluating the spin vector obtained for any surface wave that has an evanescent tail and we will discuss their different properties. Consider the metasurface shown in Fig. 1.3 where a surface wave propagates along its interface in the $z-$axis direction. The normal to the surface is in the $x-$axis. Hence, the wave vector $\mathbf{k}$ is defined as: $\mathbf{k} = k_z\hat{\mathbf{z}} + i\eta\hat{\mathbf{x}}$, where the η is the decay constant of the evanescent tail of the surface wave which is pointed in the direction normal to the surface ($x - axis$). From Maxwell's equations, we can express the general E- and H-fields of this surface wave in Gaussian units as follows [15, 16]:

$$\mathbf{E} = \frac{A_0}{\sqrt{1+\|m\|^2}}\left(\hat{\mathbf{x}} + m\frac{k}{k_z}\hat{\mathbf{y}} - i\frac{\eta}{k_z}\hat{\mathbf{z}}\right)e^{ik_z z - \eta x}, \tag{1.1}$$

$$\mathbf{H} = \frac{\mathbf{k}}{k}\times\mathbf{E} = \frac{A_0}{\sqrt{1+\|m\|^2}}\left(-m\hat{\mathbf{x}} + \frac{k}{k_z}\hat{\mathbf{y}} + im\frac{\eta}{k_z}\hat{\mathbf{z}}\right)e^{ik_z z - \eta x}, \tag{1.2}$$

where A_0 is a constant representing the field amplitude and m is a complex polarization parameter [12, 15]. The spin density vector can be expressed in terms of E and H using the following equation [12, 16]:

$$\mathbf{S} = \frac{\mathrm{Im}\{\mathbf{E}^*\times\mathbf{E} + \mathbf{H}^*\times\mathbf{H}\}}{|\mathbf{E}|^2 + |\mathbf{H}|^2}, \tag{1.3}$$

where $\mathbf{S}$ is the vector spin density normalized per one photon in units $\hbar = 1$. By substituting the E and H expressions from equations 1.1 and 1.2, the different components of the $\mathbf{S}$ vector can be written as follows:

$$S_x = 0, \quad S_y = \frac{\eta}{k_z}, \quad S_z = \frac{2Im(m)}{1+\|m\|^2}\frac{k}{k_z}. \tag{1.4}$$

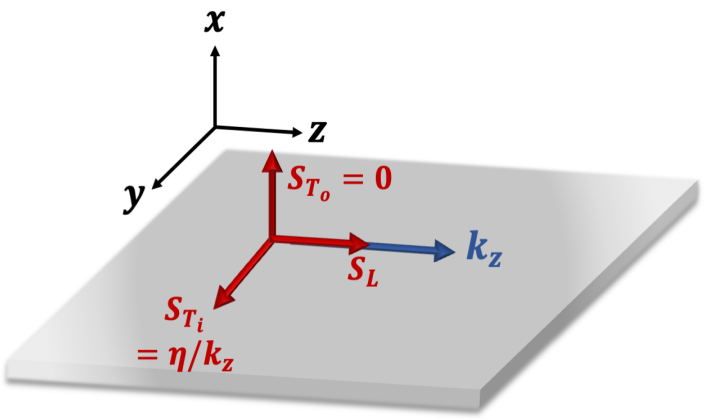

Figure 1.3: Schematic of a metasurface supporting a surface wave propagation along z-axis. The three spin components are shown where S_{T_i} and S_{T_o} are the in-plane and out-of-plane T-spins, respectively. S_L is the longitudinal spin.

Looking at the T-spin expressions, it is observed that the surface wave has a nonzero S_y, which is the in-plane T-spin, represented in Fig. 1.3 as S_{T_i} along the y-axis. However, the out-of-plane T-spin (S_{T_o}), which is S_x is zero for any surface wave. S_z, which is the longitudinal spin, is represented in Fig. 1.3 as S_L. A closer look at the expression of S_y demonstrates that the in-plane T-spin is dependent on the decay constant η, and propagation constant k. This what forms the right-hand triplet which was discussed in the previous section and shown in Fig. 1.2(c). It is also termed as spin-momentum locking. In the following Section, different designs from the literature that studied the spin-dependent wave propagation will be reviewed.

1.3 Metasurfaces and Waveguides for Spin-dependent Propagation

During the past decade, several studies were done for using photonic platforms to control the propagation direction of surface waves through altering its T-spin [17–22]. A surface wave defined as a wave propagating on a interface between metal and air that has an evanescent tail, possesses the spin-dependent propagation phenomenon due to its intrinsic T-spin as we derived in the previous Section. This spin-dependent directionality of surface waves originates from their spin-orbit coupling and can occur on any planar metal surface without any structures [23]. However, it is believed to be small and not easily observed unless enhanced by breaking the spatial inversion symmetry of the surface [17]. This can be explained by the fact that when the surface wave (which intrinsically has a T-spin) interacts with a surface of a broken mirror inversion symmetry, it will result in spin-symmetry breaking where the LCP field propagates in one direction and the RCP propagates in the opposite direction.

This has been studied in the literature in various ways including designing metasurfaces or waveguides with engineered anisotropy [17–21, 24–26], gradient metasurface designs [22, 27, 28], uniaxial hyperbolic metamaterials [29] and bandgap materials [30–32] or through inversion symmetry breaking by the near-field interference of a dipole source near the surface [33, 34] where the dipole source is placed in regions of high spin density [35]. The ability to control the directionality and polarization of SWs by engineering the metasurface designs is pivotal for many applications in valleytronics [36] and polarization-based optics such as beam splitting [37] and spin-based waveguiding [38].

The significance of the shape symmetry in controlling the polarization of the reflected and transmitted waves was explored through homogeneous and non-homogeneous designs such as V-shaped [39–41], L-shaped [42, 43] and split ring resonator metasurfaces [44, 45]. Excitation of spin-dependent guided modes can also be achieved in waveguides using scatterers [46, 47] and

quantum dots [11].

1.4 Scope of this thesis

This thesis will focus on demonstrating different designs that support spin-dependent wave propagation. We will study various designs in 1D waveguide, 2D metasurfaces and 3D photonic crystals in order to enhance spin-properties of the wave to form highly directional spin-dependent propagation. Our study investigates enhancing the spin-properties in photonic systems through three different ways: 1) dipole-dipole coupling in a multimode unit cell, 2) breaking inversion and rotational symmetry in a shape and 3) breaking the internal inversion symmetry of a 3D photonic crystal by introducing line defects.

Chapter 2 presents a numerical study of a 1D waveguide design. The waveguide design consists of a composite C-shaped metallic structure characterized by extrinsic chirality and strong transverse spin. Due to its multimode behavior, it experiences dipole-dipole coupling. We study the different modes supported by the waveguide as well as its spin properties. The spin density is calculated for each mode showing symmetry dipole coupling results in higher spin regions with which the CP dipole can efficiently couple. Field simulations are performed showing the chiral waveguide supports confined, spin-dependent unidirectional propagation with a high directionality ratio reaching 95%. Additionally, the effect of placing different local defects on the directionality of the supported guided mode is studied.

Chapter 3 presents a 2D metasurface design made of the C-shaped metallic structure. Same C-shaped design used in the 1D waveguide presented in Chapter 2 but here it is patterned as 2D metasurface design. We show numerically and experimentally that the C-shaped metasurface design provides high self-collimation due to its broken rotational symmetry which is advantageous for use in surface waveguiding. By carefully choosing its dimensions, we show we can engineer its equifrequency contour to split its surface wave into two circularly polarized waves of opposite

T-spins where the split angle can be tuned according the contour frequency. The T-spin studied here is the ordinary in-plane T-spin present for any surface. This makes the metasurface efficient for use as spin-based beam splitter. Additionally, we show that by slowly rotating the C-shaped unit cells and varying its size along the surface, we are able to steer the surface wave along a specified curved path. This work highlights the high degree of freedom achieved from using metasurface designs for manipulating the spin-orbit interaction of surface waves and providing a great control on their polarization and propagation properties.

Chapter 4 introduces a new type of surface waves, called chiral surface waves. The chiral surface waves are circularly polarized waves that possess two transverse spins, one due to out-of-plane field rotation which is intrinsic to any surface wave, and the other is due to in-plane field rotation which is enforced by the design. We show that due to strong x-to-y coupling and broken rotational symmetry of the L-shape metasurface design, it supports a chiral surface wave propagation. The two transverse spins of the chiral surface wave are locked to the momentum providing a highly confined spin-dependent propagation. This study opens a new direction for metasurface designs with enhanced and controlled spin-orbit interaction by adding an extra degree of freedom to control the propagation direction as well as the transverse spin of surface waves.

Chapter 5 explores spin-dependent propagation in a 3D system by introducing line defect. The diamond photonic crystal is studied where its band structure is calculated showing a bandgap in the microwave frequency range. By introducing a screw dislocation defect at the center of the crystal, we show that its internal inversion symmetry is broken resulting in a localized mode formed in the bandgap. By analyzing the spin-properties of the mode, we show it is spin-polarized where its spin direction follows the helicity of the screw dislocation resulting in a spin-dependent directional wave propagation. This study opens the door for manipulating and controlling spin-orbit interaction in 3D crystals through the introduction of line defects.

Finally, Chapter 6 presents a summary and concluding remarks on the thesis work. It also provide suggestions for possible future work and applications.

Chapter 2

1D Chiral Waveguide for Spin-dependent Propagation

2.1 Introduction

Chiral structures are defined as ones in which the structure and its mirror image are not superimposable by only rotations and translations. These shapes are found to produce chiroptical effects such as polarization rotation and circular dichroism [48]. However, some other structures possess extrinsic chirality in which the chiroptical effect arises when the incident wave vector does not lie on the plane of symmetry [49]. In such systems, the orientation of the incident wave together with the structure form the chiral behavior [50]. These structures provide a polarization-sensitive response to one helicity of the circularly polarized (CP) wave which is reversed when the helicity is flipped. This means that these shapes can allow only one handedness of the CP wave to propagate in one direction along the plane of illumination and the opposite handedness to propagate in the opposite direction which results in spin-dependent directionality.

In this Chapter, we introduce a metallic waveguide design that provides spin-dependent unidirectional propagation without the need to have bulk bandgap structures. The C-shaped

metallic waveguide is characterized by extrinsic chirality which when excited with a CP dipole, it enforces one handedness of the CP wave to go forward and the other handedness to go backward. We analyze the effect of placing different types of defects on the directionality of the supported chiral mode by calculating its spin density and directionality ratio.

2.2 Design and mode study

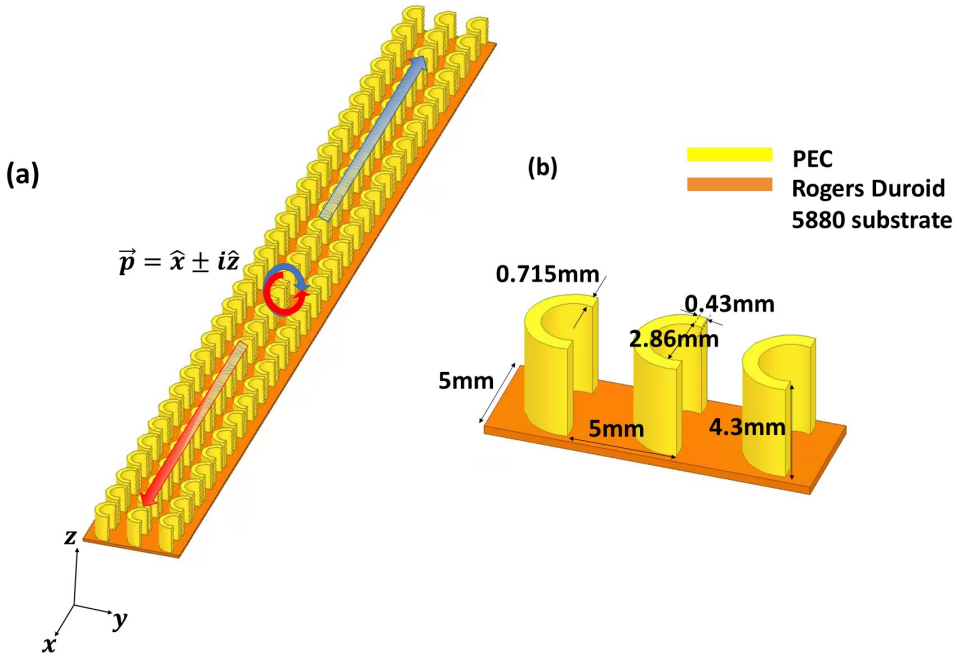

Figure 2.1: (a) Schematic representation of the unidirectional propagation of the C-shaped chiral waveguide when excited with an $\mathbf{x} \pm \mathbf{iz}$ dipole moment. (b) Dimensions of the unit cell consisting of three C shaped metallic structures placed on a Rogers Duroid 5880 substrate.

Fig. 2.1(a) shows a schematic of the C-shaped chiral waveguide design representing the spin-dependent propagation feature of the waveguide. The dipole source is placed at the center of the waveguide with a dipole moment of $\hat{\mathbf{x}} \pm \mathbf{i}\hat{\mathbf{z}}$. The dimensions of the unit cell are depicted in Fig. 2.1(b). The unit cell consists of three C-shaped metallic structures spaced 5mm

from each other placed on top of 0.381mm thick Rogers Duroid 5880 substrate ($\varepsilon_r = 2.2$). The inner diameter, thickness and height of the C-shaped metal are 2.86mm, 0.715mm and 4.3mm, respectively. The C-shaped design extends from a half circle by 0.43mm.

The design was studied and optimized numerically using Ansys HFSS. The analysis of the waveguide modes shown in Fig. 2.2 is conducted using Eigenmode simulations. As illustrated, the C-shaped waveguide is characterized by having a chiral effect which means it is sensitive to the helicity of the circular polarization of the propagating wave. The design is also a multimode as shown in the dispersion diagram presented in Fig. 2.2(c). As will be shown later, the multimode behavior allows for different spin-orbit interaction properties [35] and hence, higher degree of freedom for maximizing the spin-dependent directionality.

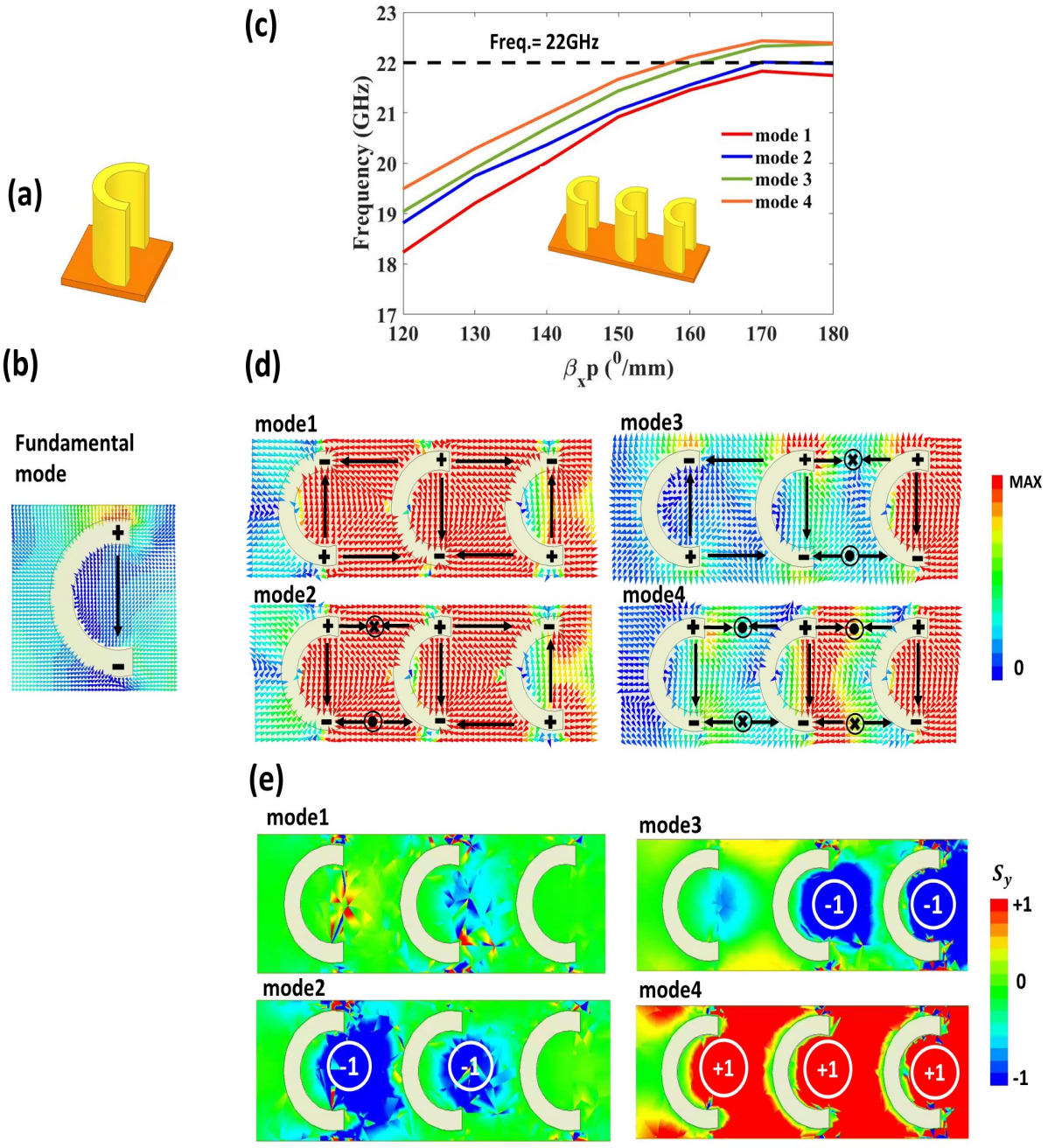

Figure 2.2: (a) Schematic of the C-shaped unit cell. (b) The vector field distribution of the fundamental mode of single C-shaped waveguide. (c) Dispersion diagram of the composite C-shaped design calculated using an Eigenmode simulation showing the first four modes of the waveguide. (d) Vector E-field distribution of the first four modes depicting the dipole-dipole coupling. The black arrows represent the direction of the E-field where + and - signs highlights the charge distribution. (e) Spin maps showing the spin density S_y where regions of high spin are highlighted.

2.3 Results

The schematic as well as the vector field distribution of the fundamental mode of a single C-shaped unit cell are shown in Fig. 2.2(a) and Fig. 2.2(b), respectively. The C-shaped metallic design has a dipole-like mode where the + and - signs represent the charge distribution and the black arrow shows the direction of the E-field. When the C-shaped metallic posts are placed near each other, dipole-to-dipole coupling between adjacent cells takes place, resulting in symmetric and antisymmetric modes. When dipoles laterally couple in the antisymmetric mode, where the adjacent dipoles have opposite directions, they attract each other decreasing the restoring force which lowers their resonance frequency [51]. This can be shown in Fig. 2.2(d) where in the first mode which has the lowest frequency, the dipoles are antisymmetrically coupled. In contrast, in the fourth mode which has the highest frequency, the dipoles are symmetrically ordered where they repel each other. Next, we investigate the spin density distribution of each mode. The spin density vector is calculated using Eq. 1.3.

Fig. 2.2(e) shows the normalized transverse spin maps (S_y) for the first four eigenmodes where high ± 1 spin density regions are highlighted. $+S_y$ corresponds to anticlockwise E-field rotation in the xz plane described as $\mathbf{E}_x - \mathbf{i}\mathbf{E}_z$ while $-S_y$ corresponds to clockwise E-field rotation described as $\mathbf{E}_x + \mathbf{i}\mathbf{E}_z$. As observed, the second, third and fourth modes show high spin density regions in the locations where symmetric dipoles coupling takes place. It can be concluded that the repulsion taking place between symmetrically ordered dipoles forces the E-field to rotate in the z-plane which results in a higher transverse spin. The high transverse density indicates higher coupling to the CP dipole sources to produce unidirectional spin-dependent propagation. The second mode is chosen to be the operating mode for this study as it can be easily excited alone reducing losses possibly encountered when more than one mode is excited. The frequency of operation is 22 GHz.

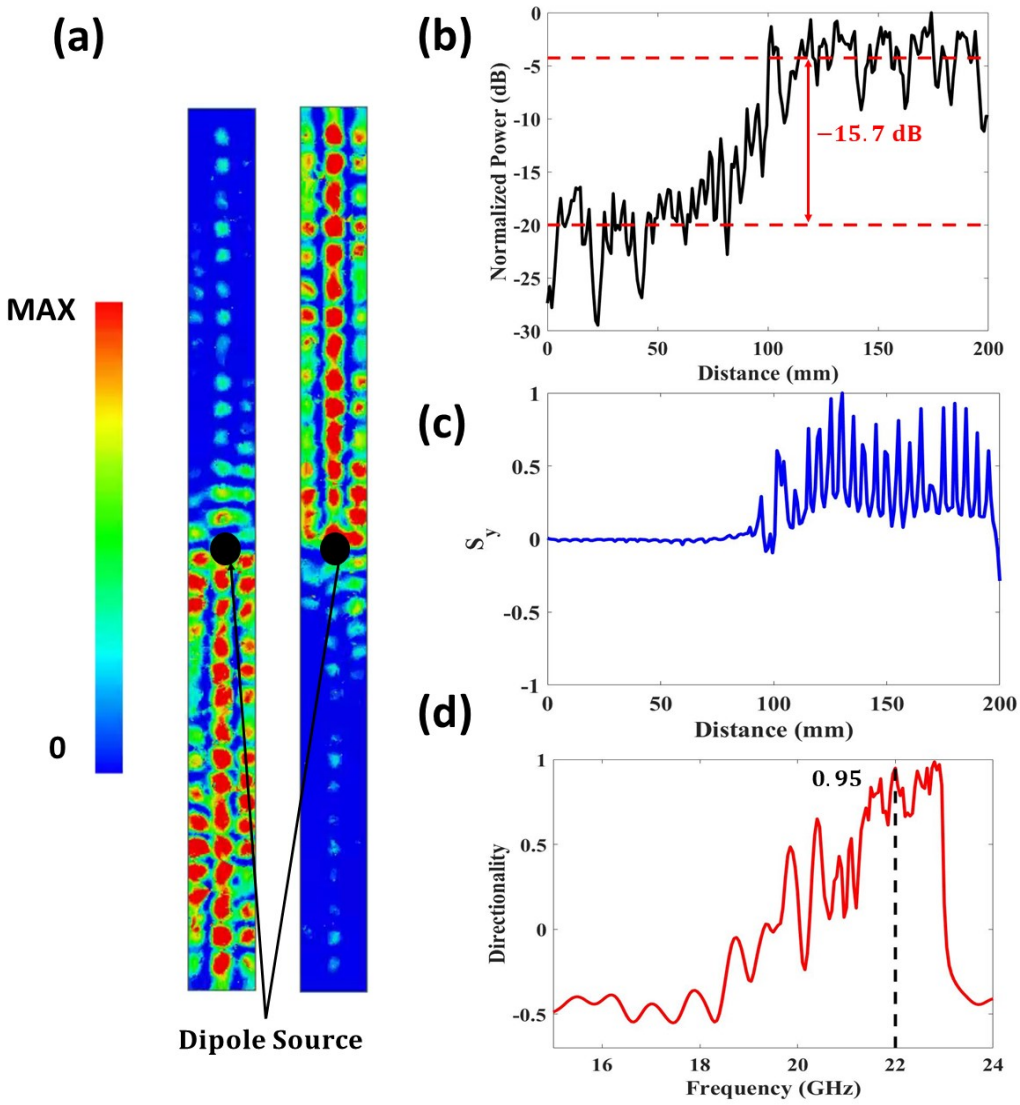

Figure 2.3: (a) Magnitude of E_z map of the C-shaped chiral waveguide at 22 GHz when excited with an $\mathbf{E}_x + \mathbf{i}\mathbf{E}_z$ dipole source (left) and $\mathbf{E}_x - \mathbf{i}\mathbf{E}_z$ dipole source (right). Unidirectionality study of the guided mode when excited with $\mathbf{E}_x - \mathbf{i}\mathbf{E}_z$ using (b) normalized power level, (c) normalized S_y and (d) Directionality calculated at a line along the center of the waveguide.

We numerically study the spin-dependent unidirectional propagation of the C-shaped waveguide using field simulations. Fig. 2.3(a) presents the E_z distribution on the waveguide when excited with an $\mathbf{E}_x + \mathbf{i}\mathbf{E}_z$ ($\mathbf{E}_x - \mathbf{i}\mathbf{E}_z$) dipole source shown on the left (right) where the dipole

source is placed at the center (marked as a black dot). To better analyze the unidirectional property of the proposed waveguide, the normalized power is plotted in Fig. 2.3(b) at a line along the center of the waveguide when it is excited with the dipole source $\mathbf{E}_x - \mathbf{iE}_z$. In which case, most of the CP wave power propagates forward and a small portion of the power goes backward. A power difference of about -15.7dB is achieved showing highly unidirectional propagation. The y-component of the spin density is presented in Fig. 2.3(c) reaching +1 in the forward direction and almost 0 in the backward direction. The unidirectional propagation can also be characterized by the Directionality ratio calculated as [11, 52]:

$$\mathbf{D} = \frac{P^f - P^b}{P^f + P^b}, \tag{2.1}$$

where P^f (P^b) is the line integration of the poynting vector calculated along the forward (backward) direction. Fig. 2.3(d) shows a directionality of 0.95 is achieved at 22 GHz.

2.4 Robustness Study against defects

Next, we investigate the effect of placing different defects on the directionality of the guided chiral mode supported by the proposed waveguide design. Fig. 2.4 presents the E-field distribution as well as the normalized spin density plots when placing different types of defects along the waveguide. As depicted in Fig. 2.4(a), the dipole source is placed at the center while the location of the defect is 57.5mm from the center. Several defect parameters are tested including the defect location (center or side), type of the scatterer (air or PEC), scaling (frequency) defect and rotation (spin-flip) defect. The results of replacing one C-shaped cell by an air gap at the center as well as on the side are shown in Fig. 2.4(b) and Fig. 2.4(c), respectively. It can be observed that the chiral mode is more sensitive to defects located at the center of the waveguide than defects located on the sides. This can be predicted from the field profile shown in Fig. 2.3(a) which shows to be confined at the center. On the other hand, replacing a C-shaped unit cell with a

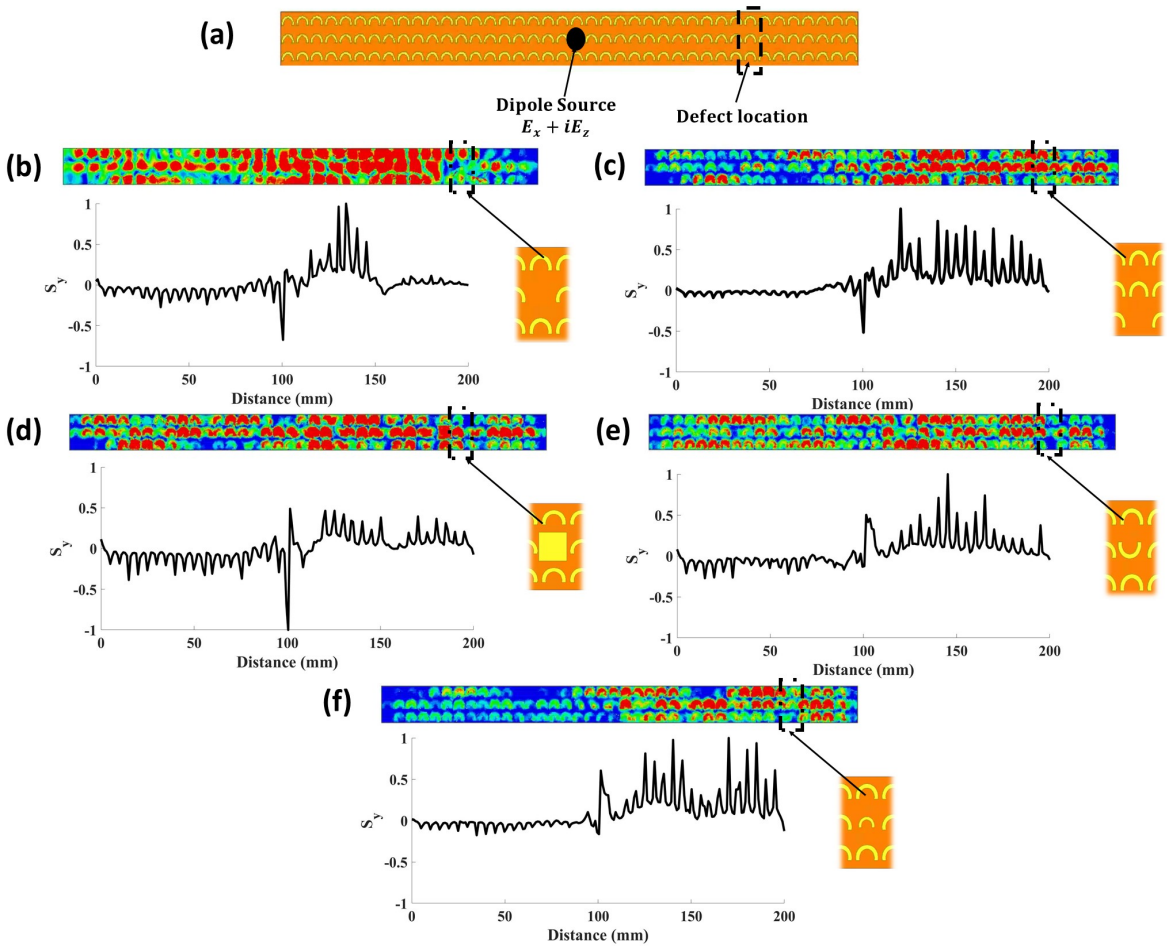

Figure 2.4: Robustness study of the C-shaped chiral waveguide against different types of defects. (a) Schematic of the waveguide showing the source and defect locations. E_z distribution and spin density (S_y) plot when (b) removing one C-shaped cell from the center, (c) removing one C-shaped cell from the side, (d) replacing the C-shaped cell at the center with a PEC scatterer, (e) rotating the C-shaped cell at the center 180^0 and (f) scaling down C-shaped cell at the center by 70%.

Table 2.1: Directionality comparison for types of defects studied throughout the Chapter.

Defect type	Directionality
None	0.97
Air gap (side)	0.8
Scaling defect (center)	0.68
Rotation defect (center)	0.33
Air gap (center)	0.22
PEC Scatterer (center)	0.1

PEC scatterer instead of an air gap results in flipping the spin of the wave which increases the backscattering as shown in Fig. 2.4(d).

Additionally, the directionality of the chiral mode was tested against rotation and scaling defects. Fig. 2.4(e) presents the result of rotating the C-shaped cell at the center 180^0 while the result of scaling down the C-shaped cell size placed at the center by 70% is presented in Fig. 2.4(f). It is observed that more backscattering takes place when placing rotation defects that result in flipping the spin of the propagating wave while less backscattering is obtained against scaling (frequency) defects. Table 2.1 displays the directionality of the C-shaped chiral waveguide calculated using Eq. (2.1) along a line across the center of the waveguide in the presence of different defects. The defect type and location have shown to influence the robustness of the chiral mode. It can be concluded that the guided chiral mode is more robust against defects occurring at the side of the waveguide than defects at the center due to the confinement of the mode profile at the center. In addition, defects that result in flipping the spin of the wave such as rotation defects and PEC scatterers produce the highest backscattering and hence the lowest directionality.

2.5 Conclusion

In this Chapter, we presented a chiral waveguide design composed of C-shaped metallic structures placed on top of Rogers Duroid 5880 substrate. The chiral waveguide when excited with a CP dipole, it results in spin-dependent unidirectional propagation with directionality ratio

of 95%. In addition, we study and compare the effect of placing different types of local defects on the spin density and the directionality of the guided mode. It is concluded that the chiral mode supported by the proposed chiral waveguide is more sensitive to defects placed at the center of the waveguide as well as defects that flip the spin direction of the CP wave such as metallic blocks.

This chapter is based on *C-shaped Chiral Waveguide for Spin-dependent Unidirectional Propagation* by S. Kandil, and D. Sievenpiper, *Applied Physics Letters*. The dissertation author was the primary author of this material.

Chapter 3

2D Metasurface for One Transverse Spin Control

3.1 Introduction

Metasurfaces provide unique capabilities in controlling the dispersion properties, phase and polarization of the propagating wave [53, 54]. This can be done by carefully choosing the unit cell design to engineer the interaction between the wave and the surface. Several research has been done to study the wide capabilities of metasurfaces from guiding [19, 55, 56], beam focusing [57, 58], splitting [59–61], steering [62], and lensing [63]. One way to control the interaction between the wave and the surface is by engineering the equifrequency contour of the unit cell design. Equifrequency contour (EFC), also called isofrequency contour (IFC), is the 2D projection of the 3D dispersion diagram at different frequencies [64, 65]. It represents a k-space map of the wave possible trajectories at different frequencies. The direction of the wave is determined by the direction of its group velocity where the group velocity of the wave is defined as $\delta\omega/\delta k$. This can be determined through the EFCs. Anisotropic shapes where some symmetries are broken have interesting, nonconventional EFCs where the contours can vary from

elliptical to flat allowing the wave to propagate in one direction (normal to the flat contour) with high self-collimation [66].

In this Chapter, we study the spin-dependent propagation achieved in a 2D metasurface version of the 1D C-shaped waveguide discussed in Chapter 2. We investigate the different ways the EFC of a metasurface can be engineered to control the surface wave propagation and spin-dependent directionality. We also show various wave properties achieved through the same metasurface design such as self-collimation, polarization-based beam splitting and wave steering. This Chapter is organized as follows: in the first Section, we discuss the homogeneous metasurface design formed of metallic C-shape unit cell, its self-collimation and spin-dependent wave propagation. In the second Section, we present the inhomogeneous design formed of the same metallic C-shaped unit cells. We discuss how its EFCs change with the rotation angle resulting in surface wave steering along two predefined paths. We study these phenomena using numerical simulations as well as experimental results which are presented in the last Section.

3.2 Homogeneous C-shaped Metasurface

Fig.3.1 presents a schematic showing the C-shaped metasurface design we will study throughout this section. As depicted in Fig.3.1(b), the unit cell consists of a metallic C-shaped of 0.143mm thickness placed on a Roger's 5880 substrate ($\varepsilon_r = 2.2$). The C-shape metallic post has a width of 0.715mm and radius of 2.145mm where its edge is extended from the center by 0.429mm. The whole surface is 250mmx250mm. The C-shape metasurface design was studied and optimized numerically using Ansys HFSS. In this section, we will explore different surface wave properties supported by the C-shaped metasurface through studying its equifrequency contours.

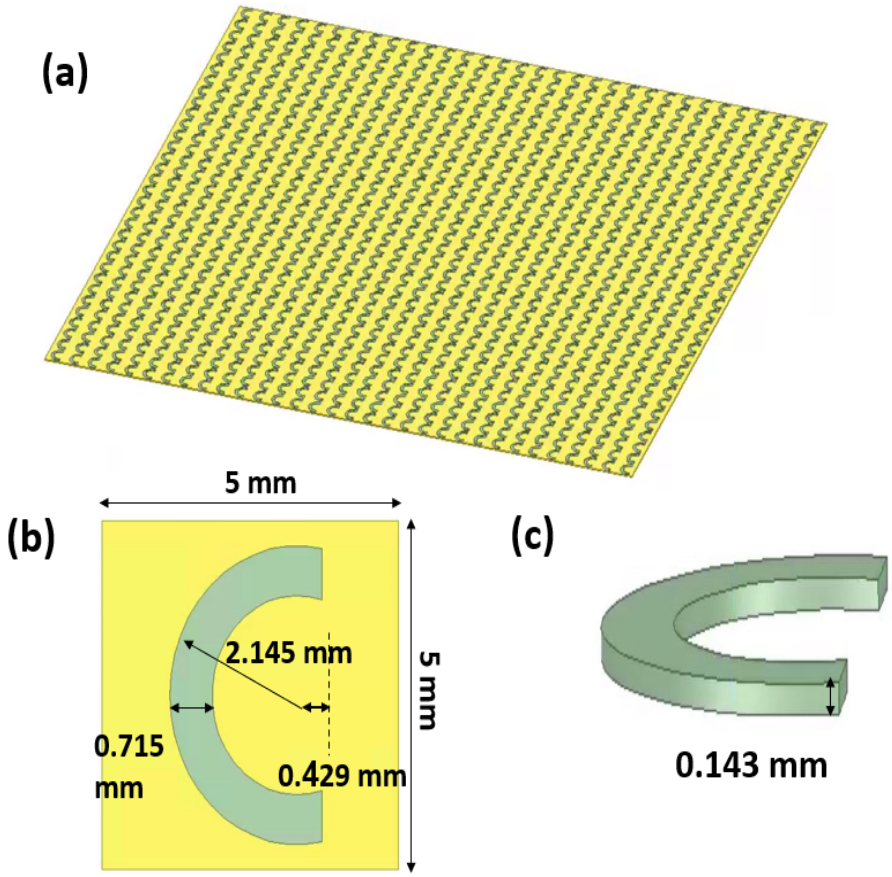

Figure 3.1: (a) Schematic showing the C-shape metasurface design. (b) The dimensions of the C-shape unit cell consisting of (d) a C-shape metallic post of 0.143mm thickness placed on a Roger's substrate.

3.2.1 Self-Collimation

Isoropic shapes with small or no asymmetry have EFC close to a circle where the wave propagates equally in all direction. As the asymmetry of the shape increases, the contour becomes flatter with higher wave directionality and hence, higher self-collimation [67]. The C-shape design has broken rotational symmetry along the z- and x-axes which makes it a low-symmetry shape and hence, have high self-collimation. This can be observed from the calculated EFC of the C-shape unit cell shown in Fig.3.2(a). It can be shown that the C-shape design possesses different contour shapes which dictate various wave propagation properties. At 14 GHz, the

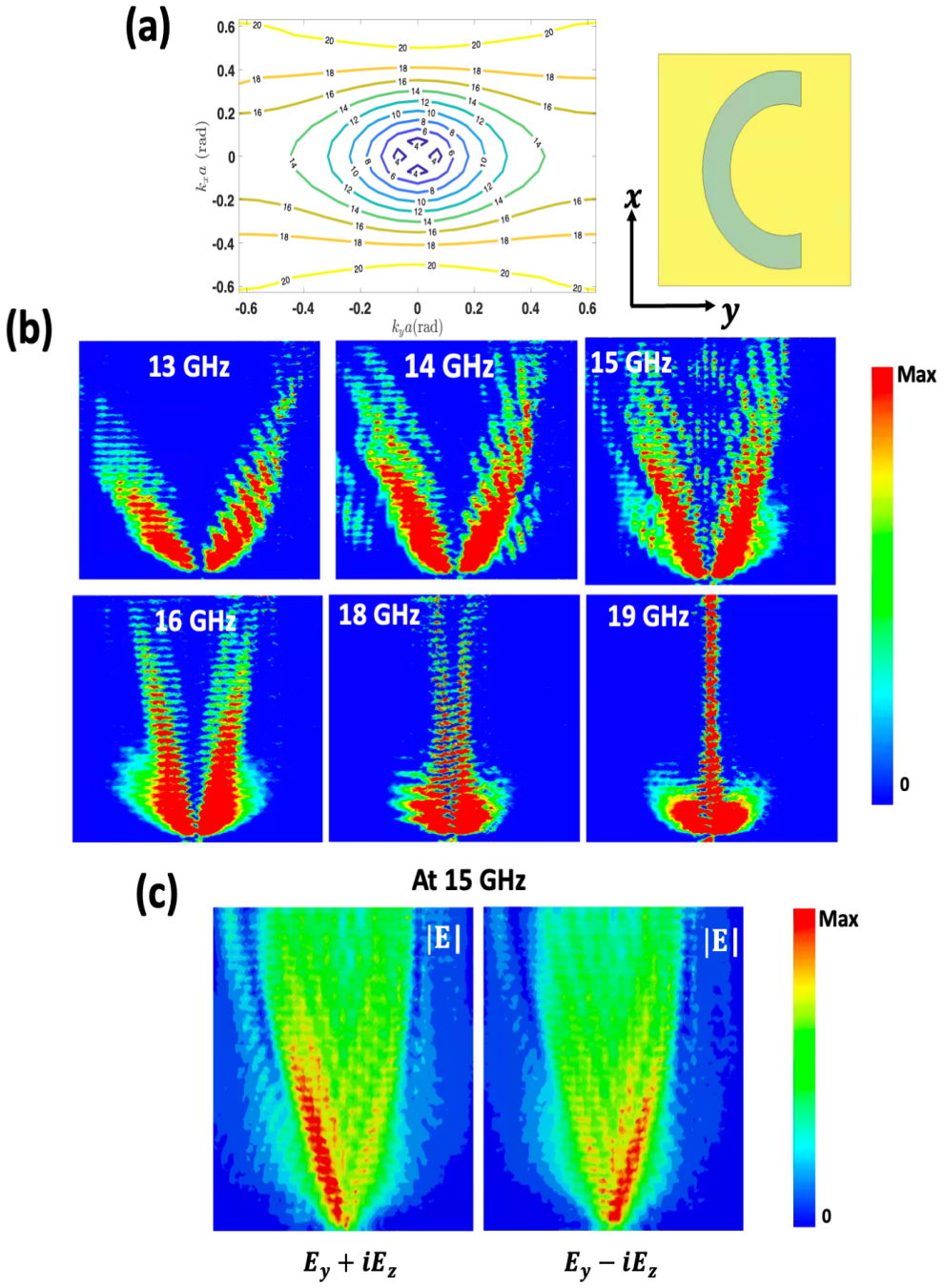

Figure 3.2: (a) EFC of the C-shape unit cell. (b) Magnitude of E_x profiles for the C-shape metasurface calculated at frequencies 13GHz to 19GHz when excited with Ey dipole source at bottom center. (c) Magnitude of E_x profiles for the C-shape metasurface calculated at 15GHz when excited at the bottom center with $E_y + iE_z$ (left) and $E_y - iE_z$ (right).

EFC is elliptical which then becomes flatter at higher frequencies where high self-collimation takes place. The E-field profiles at different frequency contours are shown in Fig.3.2(b) where the surface is excited with an E_y dipole at the bottom center. The magnitude of E_x maps are calculated for each EFC. It can be observed that the wave is split where the split angle decreases with the increase of frequency. At 19 GHz, the surface wave is highly collimated as well as spin-independent. This means that any polarization will excite the wave to propagate with high collimation and zero split angle.

3.2.2 Spin-dependent Propagation

Fig.3.2(c) shows the spin-dependent behavior of the supported surface wave. The EFC calculated for the C-shape shows a spin-based wave splitting property where the wave is split into left-handed and right-handed circularly polarized waves. By excitation of the surface with an $E_y + iE_z$ dipole source, the wave propagates along the left arm where it propagates along the right arm when excited with an $E_y - iE_z$ dipole source. The spin density is calculated using Eq. **??**. Fig.3.3(a) shows a schematic representation of the two components of the transverse spin with respect to the two wave propagation directions where the S_x component flips sign while the S_y maintains the same sign for both wave propagation directions. Fig.3.3(b) shows the numerically calculated spin maps for the two split waves for S_x and S_y.

3.3 Inhomogeneous C-shaped Metasurface

As demonstrated, the EFC is closely related to the shape of the unit cell; engineering it can be done through different ways. For example, some studies showed that the change of the unit cell from square to rectangular or parallelogram can increase the flatness of the EFCs and hence increase the collimation [68, 69]. The symmetry of the shape itself can also result in changing the contour shape. For example, as described earlier, a broken rotational symmetry can

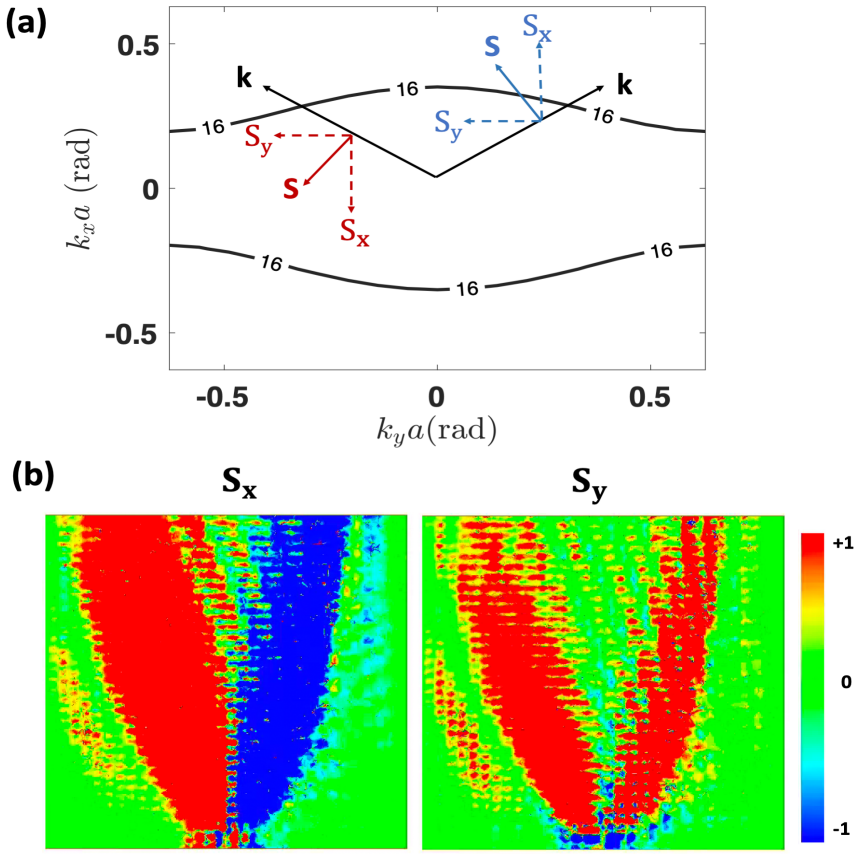

Figure 3.3: (a) The 16GHz EFC of the C-shape unit cell where the k-vector directions and transverse spin components are depicted. (b) The x-component (left) and y-component (right) of the transverse spin density vector for the surface wave supported by the C-shape metasurface at 16GHz.

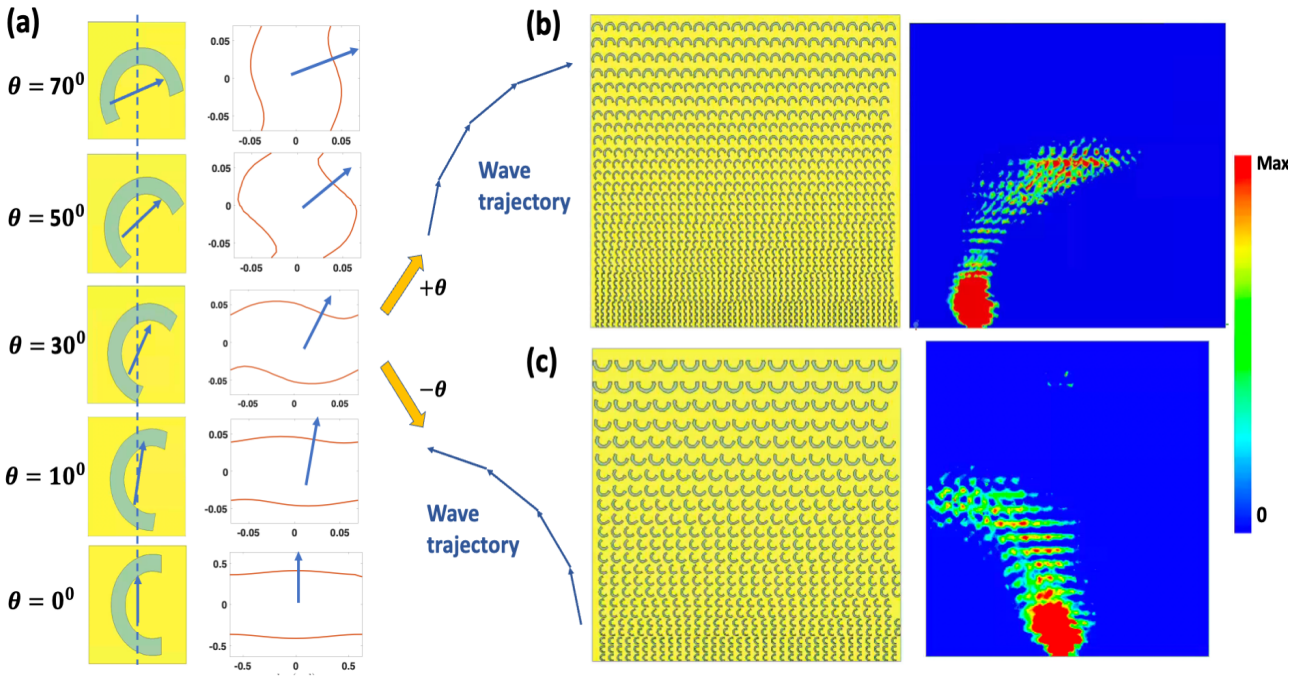

Figure 3.4: (a) Schematics showing the rotated C-shape unit cells at rotation angle (θ) from 0^0 to 70^0 and their corresponding EFCs. The two wave trajectories formed when θ is positive and negative are demonstrated. The designed Inhomogeneous C-shape metasurface designs and their calculated E-field profiles show to steer the surface wave along a curved path towards (b) the right and (c) the left at 19GHz when excited with $E_y - iE_z$.

produce flatter contours along the x- or y-axis. 45^0 mirror symmetry of a shape can result in tilted contours [70].

In recent decades, there has been a great interest in gradient metasurfaces which are non-periodic surfaces aimed for wavefront manipulation for beam steering applications in near- or far-fields [71]. Such surfaces can be designed using ray optics approach [72], equivalence principle (Huygens metasurfaces) [73], geometric phase approach [74] or using programmable design generation [75]. Here, we present an alternative approach to design such surfaces by engineering EFCs. We show that we are able to steer the surface wave to propagate smoothly along specified curved paths using an inhomogeneous metasurface made of rotated C-shape unit cells. The inhomogeneous design is simply done by mapping the rotated C-shapes and their angle of collimation using the EFCs to form the specified wave path.

3.3.1 Rotation Angle and EFC

Fig.3.4(a) shows the design steps to make the inhomogeneous metasurface designs shown in Fig.3.4(b) and (c) through engineering the EFC. With a focus on the C-shape's highly collimated EFC, it can be shown that rotating the C-shape unit cell results in rotating its EFC by almost the same angle of rotation, θ. For simplicity, we show schematics of five rotated unit cells at $\theta = 0^0$ to $\theta = 70^0$ and their corresponding EFCs. The blue arrows indicate the propagation direction of the wave. The wave trajectory deduced from the EFCs of the rotated C-shapes when using positive θ values can be shown in Fig.3.4(a), top right while the wave trajectory for using negative θ values where the wave is steered to the left is shown in Fig.3.4(a), bottom right.

Fig.3.4(b) and (c) show the inhomogeneous metasurface designs for the two wave paths described earlier. The design shown in Fig.3.4(b) is composed of 30 columns divided into 9 groups. In each group, θ is incremented by 10^0 and the shape is scaled up by a scaling factor, s. This is due to the fact that rotating the unit cell results in slight increase in its supported surface wave frequency. To eliminate the frequency mismatch, each rotated C-shape is scaled up by a

scaling factor of 1.11. This scaling factor is deduced from mapping the rotation angles and its resulting frequency shift. The scaling factor, s, of a unit cell can be defined in terms of its rotation angle as follows:

$$s = 1.11^{\frac{\theta}{10}}. \tag{3.1}$$

3.3.2 Surface Wave Steering

The E-field profiles for the two inhomogeneous metasurface designs at 19GHz are presented on the right in Fig.3.4(b) and (c) showing the smooth steering of the surface wave along curved paths. The demonstrated steered wave is spin-independent since we worked with the highly-collimated, spin-independent contour. This means that the same E-field profile can be achieved with a linearly or circularly polarized excitation source. This demonstrates how the EFC engineering for wave steering provides the capability of smoothly steering the surface wave along predetermined paths without much complexity in the designing process where the same unit cell design is used.

3.4 Experimental Results

The C-shape metasurface was fabricated and measured. Fig.3.5(a) shows a photo of the fabricated homogeneous C-shape metasurface while the inhomogeneous surface is shown in Fig.3.5(d). The C-shape structures are made of copper which are placed on top of a Roger's 5880 substrate of thickness 0.381mm. An E_y probe used to excite the surface which is placed at the bottom center. Another measuring probe, E_x is attached to a moving station which scans the surface point by point. Both probes are connected to Vector Network Analyzer (VNA) where the magnitude and phase of S21 are measured. The magnitude and phase of the E_x can be extracted for the whole surface at different frequencies showing the different wave propagation properties as shown in Fig.3.5(b) which match the simulation results shown in Fig.**??**(b). The E-field profile

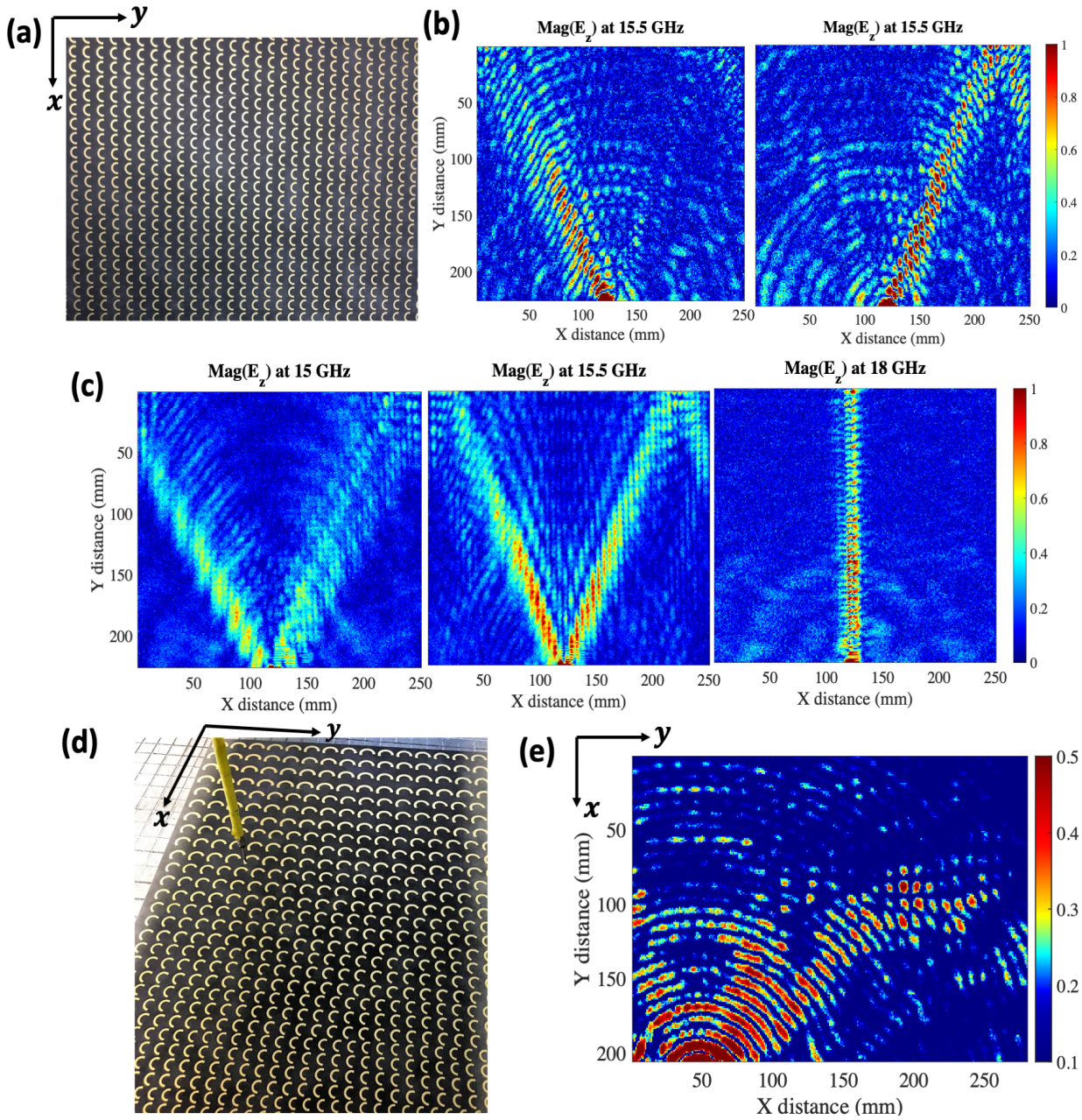

Figure 3.5: (a) Photo of the fabricated C-shape metasurface. (b) Measured E_x field maps at frequencies 15GHz to 18GHz showing the different wave split angles when excited with E_y where the highly collimated wave propagation is shown at 18GHz. (c) The measured Ex for the C-shape metasurface at 15.5GHz when excited with $E_y + iE_z$ (left) and $E_y - iE_z$ (right) at the bottom center showing the spin-dependent propagation behavior. (d) Photo of the fabricated inhomogeneous C-shape metasurface. (e) The measured E_x profile showing the surface wave propagation along a curved path.

shown on Fig.3.5(c) is measured for the homogeneous C-shape surface at 15.5GHz when excited with a circularly polarized (CP) dipole source. The CP dipole excitation is done through excitation with an E_y and E_z dipole sources separately and collecting the magnitude and phase of E_x scan for each excitation. The two scans are then added with a 90^0 phase shift using the following equation:

$$\mathbf{E}_{\mathrm{x}}^{y} \pm i\mathbf{E}_{\mathrm{x}}^{z} = |\mathbf{E}_{\mathrm{x}}^{y}| \cos\left(\phi_{\mathrm{x}}^{y}\right) + |\mathbf{E}_{\mathrm{x}}^{z}| \cos\left(\phi_{\mathrm{x}}^{z} \pm 90^{0}\right), \tag{3.2}$$

where $\mathbf{E}_{\mathrm{x}}^{y(z)}$ is the measured $\mathbf{E}_{\mathrm{x}}$ when excited with a probe along $y(z)$-axis. The E_z profile is measured for the inhomogeneous metasurface at 18.5GHz and shown in Fig.3.5(d) which demonstrates the surface wave steering along the predefined path.

3.5 Conclusion

In this Chapter we studied numerically and experimentally a metallic C-shape metasurface design and its various wave propagation and polarization properties. We showed that due to the broken rotational symmetry of the C-shape design, it possesses high self-collimation. Additionally, we studied the spin-momentum locking phenomenon in the C-shape by calculating its spin density and showed it is capable of spin-dependent wave splitting. We also showed two inhomogeneous metasurface designs to steer the wave along defined curved paths by rotating the C-shape EFCs and scaling their sizes to eliminate frequency mismatch. This work emphasizes that engineering the EFCs can be simply done to achieve wide wave properties: spin-dependent wave splitting steer, highly confined waveguiding and wave steering along defined paths.

This chapter is based on *Engineering Equifrequency Contours of Metasurfaces for Self-Collimated Surface Wave Steering* by S. Kandil, D. Bisharat and D. Sievenpiper, *In preparation*. The dissertation author was the primary author of this material.

Chapter 4

2D Metasurface for Two Transverse Spin Control

4.1 Introduction

In the previous Chapter, we showed the different wave and spin properties that can be achieved through design engineering of metasurfaces. However, the surface wave supported by the design studied has only one transverse spin which is an in-plane spin resulting from out-of-plane field rotation. In this Chapter we introduce a new type of SW supported by a metallic surface called a chiral SW (CSW). CSW is defined as a SW that possesses two T-spins, an in-plane T-spin which is inherent to any SW and an out-of-plane T-spin which is formed due to the in-plane field rotation that is enforced by the metasurface design. We show that this additional in-plane field rotation can be induced solely by the symmetry properties of the metasurface unit cell without applying magnetic fields.

We study analytically and experimentally an L-shaped metasurface design that supports CSW. We show that due to its 45^0 mirror inversion symmetry and broken rotational symmetry, its supported mode possesses an out-of-plane T-spin in addition to its in-plane T-spin. Both

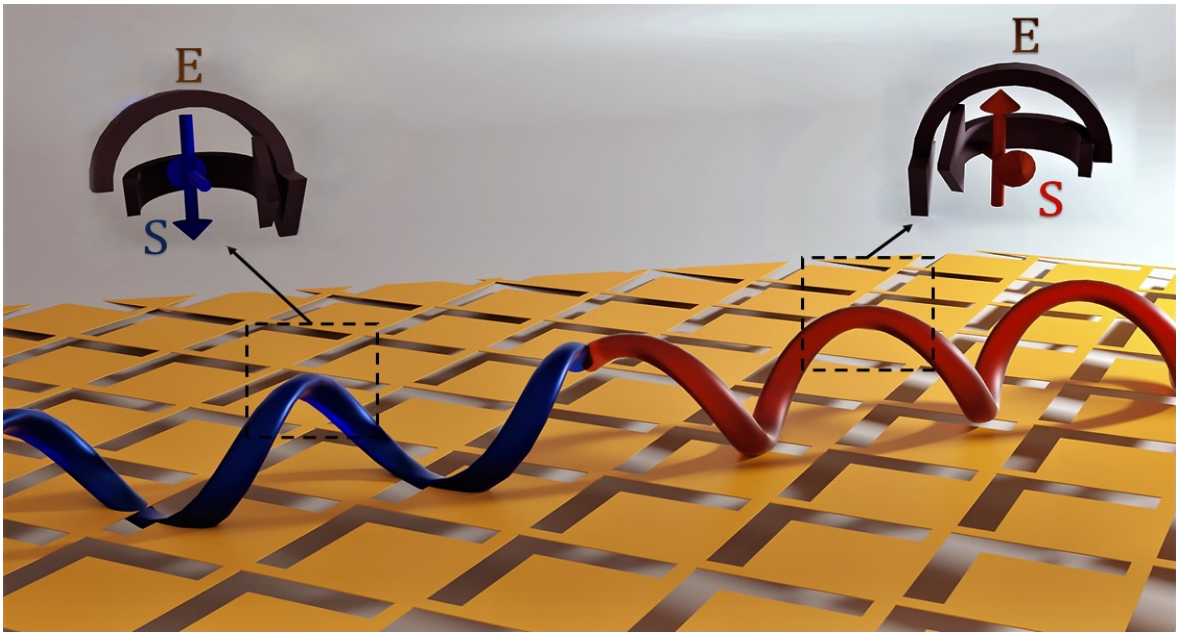

Figure 4.1: Schematic representation of the CSW propagation on the L-shape metasurface showing the two T-spins which both flip sign when the propagation direction is reversed.

T-spins are locked to the propagation direction of the SW resulting in spin-dependent directional propagation. This work provides a platform with an extra degree of freedom for controlling the spin-orbit interaction of SWs by adding a new T-spin. It also means that the CSW can be excited using a circularly polarized (CP) source that is in the transverse plane (xz) as well as in the same plane as the surface (xy), which is more practical to demonstrate in experiments. This study opens a new direction for metasurface designs with enhanced and controlled spin-orbit interaction by adding an extra degree of freedom to control the propagation direction as well as the transverse spin of surface waves.

4.2 Design and Results

Fig. 4.1 shows a schematic representation of the CSW propagation on the L-shaped metasurface when excited with a linearly polarized source at the center. For more details on the design and dimensions of the metasurface and the L-shape unit cell, see Figure S1 of the

Supporting Information. As depicted, the CSW possesses two T-spins due to in-plane and out-of-plane E-field rotations. The SW propagates along the diagonal of the metasurface where the two spins flip when the momentum is reversed demonstrating the spin-momentum locking feature. The metasurface consists of a metallic sheet from which an L-shape periodic pattern is etched.

The significance of CSWs is that unlike other SWs, their T-spin direction is enforced and controlled by the design and is not intrinsic to the wave itself which provides an additional degree of freedom to tailor it. Here, we explain in terms of analyzing the L-shape design, the design characteristics that can support CSWs.

4.2.1 45^0 Mirror Inversion Symmetry

Chirality of an object is defined as being not superimposable with its mirror image [49,76]. On the other hand, the chirality of the wave is defined as having rotating electric or magnetic fields (RCP or LCP) while propagating. The magnitude and direction of the chirality of light can be calculated using the vector spin density, S, defined in Eq. 1.3. SWs that are TE or TM are proved to already possess out-of-plane field rotations resulting in an in-plane T-spin [12]. For the design to support an additional out-of-plane T-spin, it has to enforce an in-plane E-field or H-field rotation. As will be shown later, the design does not have to be chiral to support this chiral mode but it has to have strong *x*-to-*y* coupling, which refers to the ability of the design to induce a y-polarized E-field when excited with an x-polarized dipole source and vice-versa.

The L-shape is characterized by two key features that make it ideal for supporting an out-of-plane transverse spin-splitting leading to confined spin-dependent propagation. First, it has $\pm 45^0$ mirror symmetry with respect to the *xz*- and *yz*- planes which results in having a non-zero *x*-to-*y* coupling [77] as depicted in the schematic of the L-shape unit cell shown in Fig. 4.2(a) where *a* is the periodicity of the L-shape square unit cell. This can also be viewed as coupling between two orthogonal dipole modes. It is important to note that since the L-shape possesses a mirror symmetry, it is not a chiral structure. The electric *x*-to-*y* coupling factor can be represented

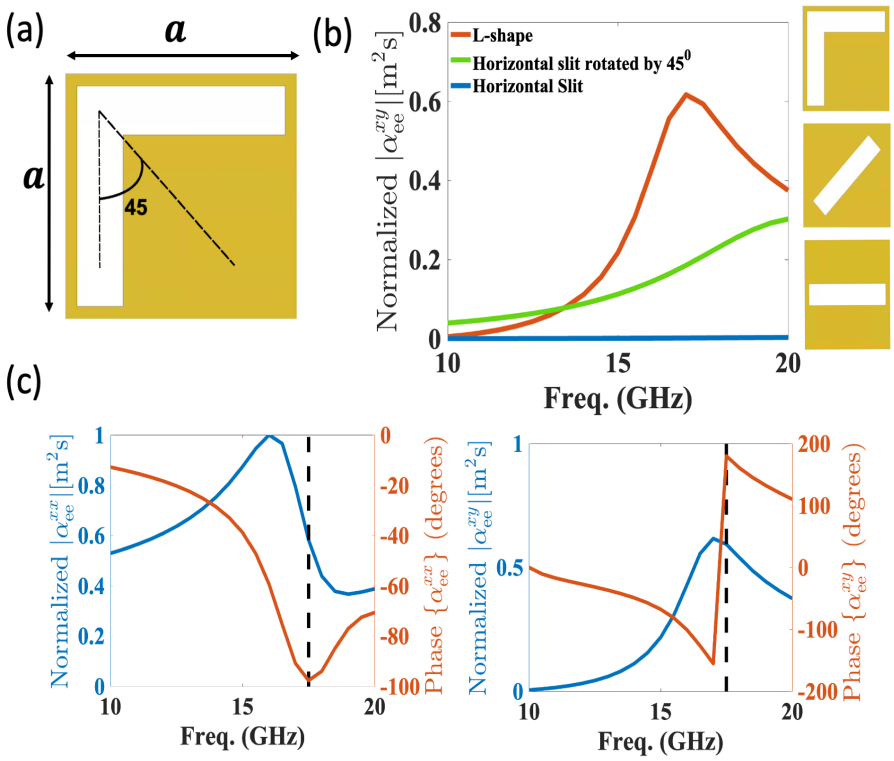

Figure 4.2: (a) Schematic of the L-shape unit cell showing its 45^0 mirror symmetry. (b) Comparison of the extracted normalized magnitude of α_{ee}^{xy} for the L-shape, slit rotated by 45^0 and horizontal slit. (c) Extracted normalized magnitude and phase of the α_{ee} tensor components of the L-shape. The vertical dotted line highlights the mode frequency 17.5GHz.

by the electric polarizability, α_{ee}^{xy} (or α_{ee}^{yx}), which is a component of the electric polarizability tensor defined in the following equation:

$$\mathbf{p} = \overline{\overline{\alpha}}_{\text{ee}}.\mathbf{E}_{\text{inc}} + \overline{\overline{\alpha}}_{\text{em}}.\mathbf{H}_{\text{inc}}, \tag{4.1}$$

where $\mathbf{p}$ is the electric dipole moment and $\mathbf{E}_{\text{inc}}$ and $\mathbf{H}_{\text{inc}}$ are the incident electric and magnetic fields, respectively. $\overline{\overline{\alpha}}_{\text{ee}}$ and $\overline{\overline{\alpha}}_{\text{em}}$ are the electric and electro-magnetic polarizability tensors, respectively. For simplicity, we assume we only excite with an electric dipole so only $\overline{\overline{\alpha}}_{\text{ee}}$ will be

considered throughout this study. The $\overline{\overline{\alpha}}_{ee}$ is described as:

$$\overline{\overline{\alpha}}_{ee} = \begin{bmatrix} \alpha_{ee}^{xx} & \alpha_{ee}^{xy} \\ \alpha_{ee}^{yx} & \alpha_{ee}^{yy} \end{bmatrix} \tag{4.2}$$

For clarification, Fig. 4.2(b) shows a comparison of the normalized magnitude of α_{ee}^{xy} for three different shapes: horizontal slit, slit rotated by 45^0 from the horizontal axis and the L-shape. The polarizability tensor is calculated using the formulations and code presented in [78]. As is observed, the three shapes are achiral. The horizontal slit has a very small α_{ee}^{xy} of 2.4 x 10^{-3} which can be approximated to zero in comparison to the latter two shapes which have 45^0 mirror symmetry and therefore their α_{ee}^{xy} is higher, 0.3 for the 45^0 rotated slit and 0.6 for the L-shape. Comparison to other shapes is shown in the supporting information, Figure S8. A large *x*-to-*y* coupling is essential for the shape to support in-plane E-field rotation as will be derived here. The dimensions of the L-shape used in this study are as follows: the periodicity *a* is 5mm and the length and width of the slits are 4.5 mm and 1 mm, respectively. The $|\alpha_{ee}^{xy}|$ of the L-shape has a peak value around 17.5 GHz which is the resonance frequency where the chiral surface mode is found to be excited.

Fig. 4.2(c) shows the extracted normalized magnitude and phase of the *xx* and *xy* components of the α_{ee} tensor for the L-shape unit cell. $\alpha_{ee}^{yy} = \alpha_{ee}^{xx}$ and $\alpha_{ee}^{yx} = \alpha_{ee}^{xy}$ due to the symmetry of the system, where the L-shape has equal arm lengths along x- and y-directions. It is observed that at the resonance frequency of the L-shape, 17.5 GHz, the tensor components have equal magnitudes of 0.6 while the phases are -90^0 for α_{ee}^{xx} (and α_{ee}^{yy}) and 180^0 for α_{ee}^{xy} (and α_{ee}^{yx}). The magnitudes and phases of $\overline{\overline{\alpha}}_{ee}$ can be substituted in Eq. 4.2 giving the following matrix:

$$\overline{\overline{\alpha}}_{ee} = \begin{bmatrix} -i0.6 & -0.6 \\ -0.6 & -i0.6 \end{bmatrix} \tag{4.3}$$

By substituting Eq. 4.3 in Eq. 4.1, the electric dipole moment can be written as:

$$\mathbf{p} \propto -\mathrm{E}_{\mathrm{inc}}^{x}\left(i0.6\widehat{\mathbf{e}}_{\mathrm{x}}+0.6\widehat{\mathbf{e}}_{\mathrm{y}}\right)-\mathrm{E}_{\mathrm{inc}}^{y}\left(0.6\widehat{\mathbf{e}}_{\mathrm{x}}+i0.6\widehat{\mathbf{e}}_{\mathrm{y}}\right). \tag{4.4}$$

From Eq. 4.4, one can conclude that an in-plane E-field rotation is supported by the L-shape when excited with x-polarized ($\mathrm{E}_{\mathrm{inc}}^{y}=0$) or y-polarized ($\mathrm{E}_{\mathrm{inc}}^{x}=0$) dipole source. Hence, the following condition can be derived for the metasurface design to induce an in-plane circularly polarized mode:

$$\alpha_{ee}^{xx}=\pm i\alpha_{ee}^{xy}. \tag{4.5}$$

4.2.2 Broken Rotational Symmetry and Spin-splitting

Secondly, the L-shape has broken rotational symmetry. It was shown in the literature that the broken rotational symmetry of the metasurface can result in spin-dependent splitting in the momentum space by inducing an additional geometric phase for LCP incidence with respect to RCP incidence [22, 79, 80]. For simplicity, the x and y axes are rotated by 45^0 in the clockwise direction in which the modified axes are x' and y' where x' represents the longitudinal direction and y' represents the in-plane transverse direction. In Fig. 4.3(a) and 4.3(c), we show the spin-splitting in k-space along the two transverse directions, y' and z, by calculating the integral spin density, S^I, defined as:

$$S_{y'}^{I}(k_x,k_y)=\int_{x=0}^{x=a}\int_{y=0}^{y=a}S_{y'}(x,y,k_x,k_y)\,dx\,dy \tag{4.6}$$

$$S_{z}^{I}(k_x,k_y)=\int_{x=0}^{x=a}\int_{y=0}^{y=a}S_{z}(x,y,k_x,k_y)\,dx\,dy \tag{4.7}$$

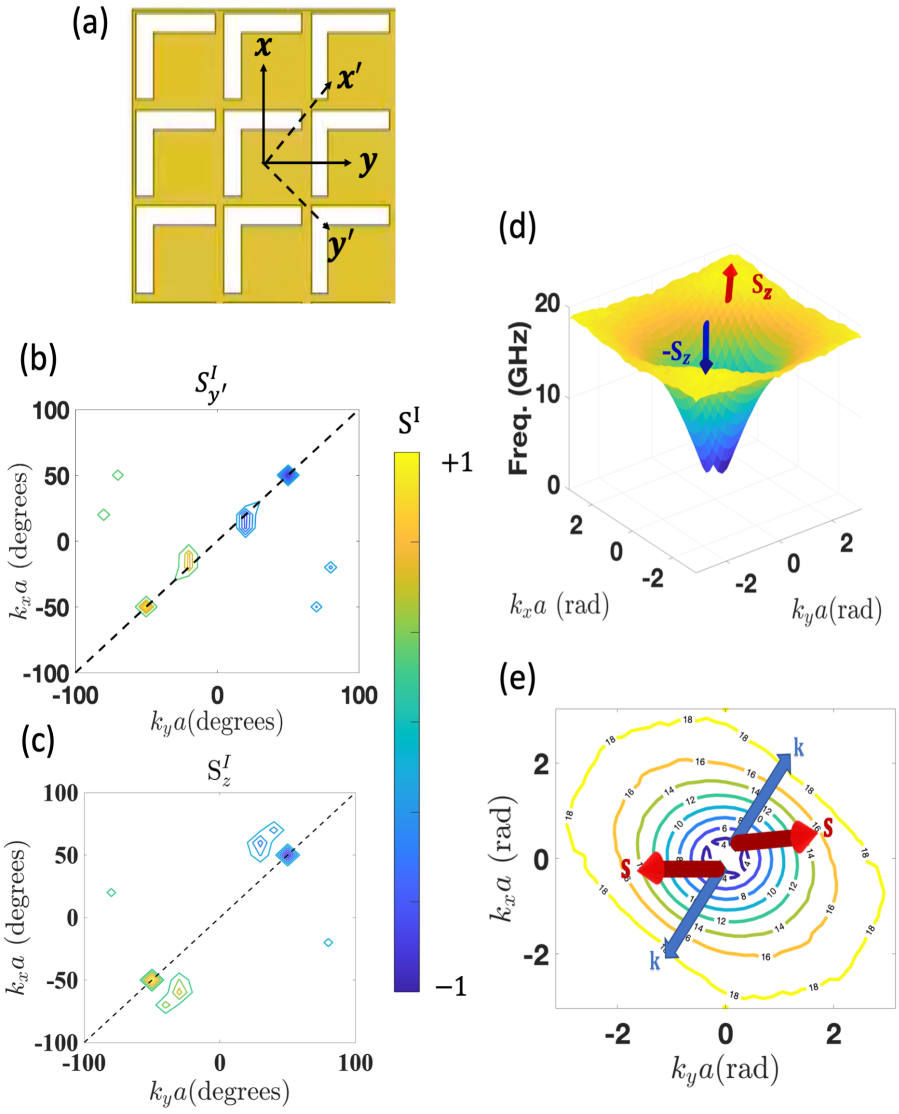

Figure 4.3: (a) Schematic of the L-shape surface showing the original $x-y$ axes as well as the modified $x'-y'$ axes (the $x-y$ rotated by 45^0 in the clockwise direction). Numerically calculated maps of the normalized integrated transverse spin number in k-space in (b) y', and (c) z directions. (d) The numerically calculated 3D dispersion diagram of the L-shape and (e) its EFC using eigenmode simulation where the k-vector directions are presented showing a diagonal surface wave propagation.

where $S_{y'}$ and S_z are y' and z components of the spin density calculated using Eq. (**??**). The integral spin densities are evaluated numerically using the eigenmode solver by integrating over the surface area of the L-shape unit cell at different points in the 2D k-space $(k_x a, k_y a)$ to generate the spin maps presented in Fig. 4.3(b) and 4.3(c). The $S^I_{y'}$ represents the in-plane transverse spin

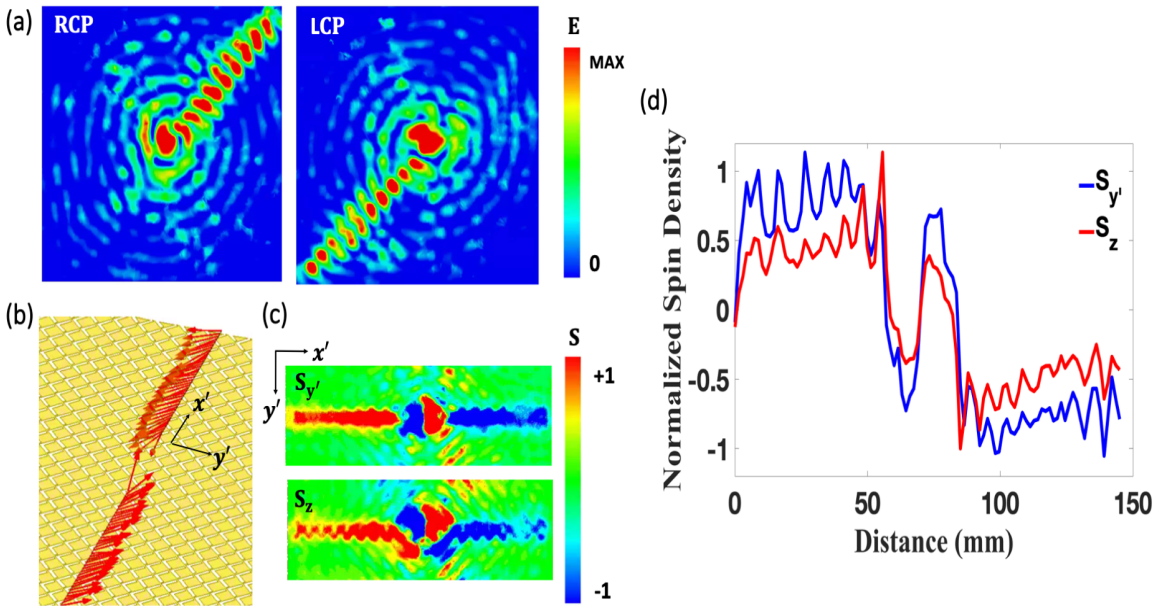

Figure 4.4: (a) Magnitude of the E-field map of the L-shape metasurface at 17.5GHz GHz when excited with an $\mathbf{E}_x + i\mathbf{E}_y$ dipole source (left) and $\mathbf{E}_x - i\mathbf{E}_y$ dipole source (right). Spin density study of the chiral wave when excited with E_x: (b) The calculated vector spin density showing that the direction of spin flips as the propagation direction is reversed. (c) Normalized $S_{y'}$ and S_z 2D maps and (d) normalized T-spins calculated plotted at a line along the diagonal of the metasurface.

while S_z^I represents the out-of-plane transverse spin. The in-plane as well as the out-of-plane transverse spins splitting can be observed where the orange contours indicate positive S^I (spin up) while the blue ones indicate a negative S^I (spin down). It can be shown that the spins split along the diagonal plotted as a dotted line at the same k-coordinates of $(-50^0, -50^0)$ (spin-up) and $(50^0, 50^0)$ (spin-down). This means that the two transverse spins will be supported by the SW having a propagation constant matching these k-coordinates. The diagonal line here corresponds to the direction of the propagation of the chiral mode $(\widehat{\mathbf{e}}_x + \widehat{\mathbf{e}}_y)$ where the spin-momentum locking takes place. This spin-splitting in k-space results in spin-dependent propagation in real space as will be shown later.

4.2.3 Self-Collimation of L-shape

Additionally, the L-shape metasurface is characterized by having high self-collimation. Self-collimation is a property intensely studied for photonic crystals and it arises due to special dispersion characteristics in which the wave is forced to propagate in a confined direction without spreading [64]. This is usually represented by a flat equifrequency contour (EFC). Breaking the rotational symmetry of the lattice unit cell has previously shown to produce high self-collimation and tilted EFCs [81]. This can be shown for the L-shape in the flat EFC presented in Fig. 4.3(e). The EFC can be obtained by slicing the 3D dispersion diagram shown in Fig. 4.3(d) at different frequencies. Both are calculated numerically using eigenmode simulations. More information on the dispersion diagram of the L-shape and the supported surface mode frequencies can be found in the supporting information. The Poynting vector of the SW can have different directions depending on the curvature of the EFC. The flatter the contour, the higher the self-collimation is since the wave is then forced to propagate in a single direction that is normal to the flat contour. As shown in Fig. 4.3(b), the EFCs of the L-shape are found to be tilted at an angle of 45^0 from the y-axis verifying the k-vector direction along $(\widehat{\mathbf{e}}_x + \widehat{\mathbf{e}}_y)$ as concluded earlier from the integral spin density maps.

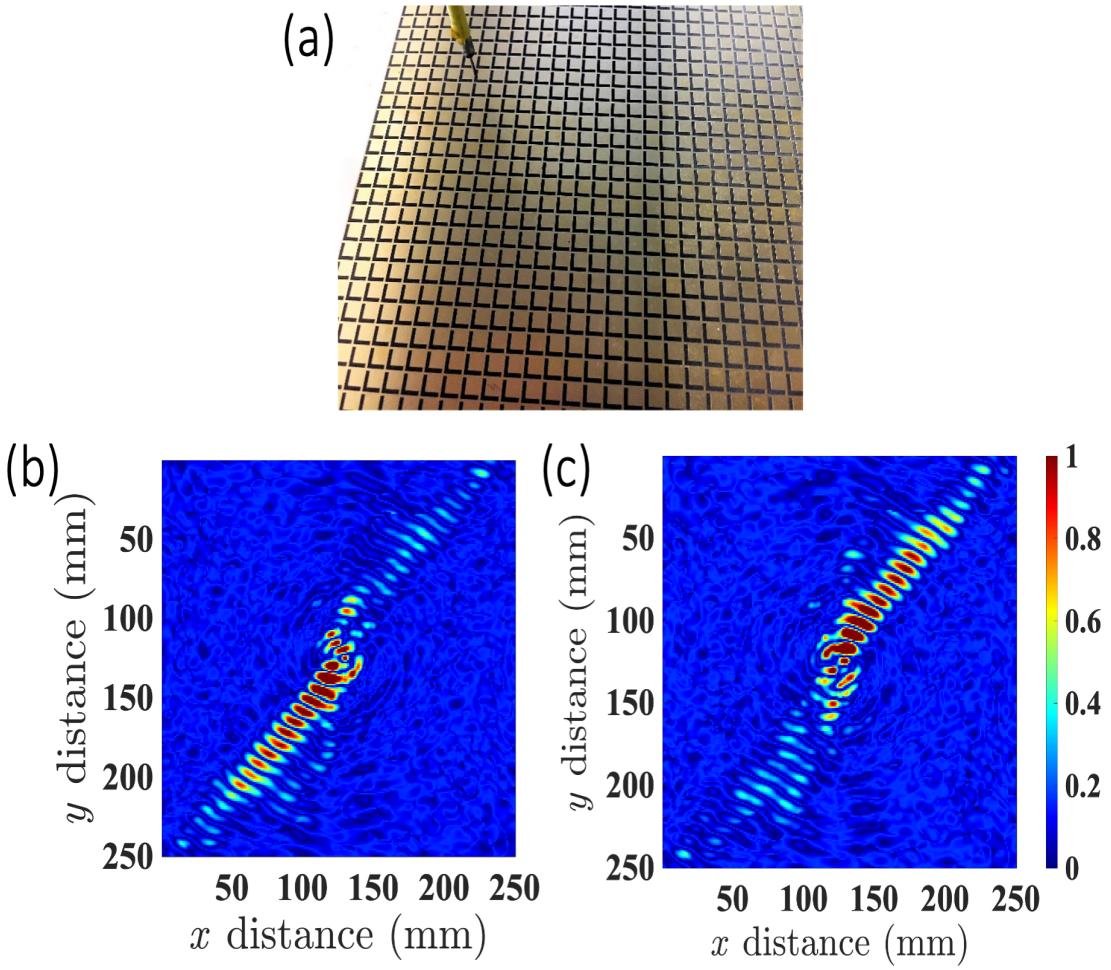

Figure 4.5: Measurement results of the L-shape metasurface. (a) A photo showing the measurement setup where a probe antenna oriented along the z-axis is used to measure the E-field distribution. An x and y probes were used for the excitation. Normalized magnitude of the E_z distribution measured at 14.5 GHz when excited at the center with an equivalent excitation of (b) $\mathbf{E}_x - i\mathbf{E}_y$ and (c) $\mathbf{E}_x + i\mathbf{E}_y$

The L-shape metasurface is numerically simulated using Ansys HFSS. Fig. 4.4(a) shows the simulated E-field distribution at 17.5GHz where the surface is excited with an in-plane CP source at the center described as $\mathbf{E}_x \pm i\mathbf{E}_y$. The polarization-dependent unidirectional propagation feature of the CSW is depicted where an RCP source excites a surface mode that propagates only forward along the diagonal (left) while an LCP source excites a surface mode propagating only backward (right). It's important to note that the L-shape metasurface is not broadband. By analyzing the 3dB bandwidth, it is found to be 1.2GHz (see Supporting information, Figure S3).

The spin density is calculated using Eq. (1.3) for the CSW and is presented in Figs. 4.4(b), 4.4(c) and 4.4(d). The spin density vector is shown in Fig. 4.4(b), calculated when the surface is excited with a x-polarized dipole source at the center of the surface. The two induced T-spins are then along y' and z axis. The normalized magnitudes of $S_{y'}$ (in-plane T-spin) and S_z (out-of-plane T-spin) are shown as color maps in Fig. 4.4(c) and along a line across the diagonal in Fig. 4.4(d). Further analysis on the strengths of each T-spin as well as the phase shift between the two E-field components of each T-spin is demonstrated in the Supporting Information. The spin-momentum locking feature is clearly observed from the numerically calculated spin density of the CSW for the two T-spins. It is important to note that the resulting spin-momentum locking taking place for each of the two T-spins is due to different origins. The in-plane T-spin which is intrinsic to any SW follows the spin-momentum locking rule defined from Maxwell's equations by the right-hand triplet formed of spin, propagation constant and decay constant. On the other hand, the out-of-plane T-spin is enforced and controlled by the symmetry properties of the L-shape. This means that when the propagation direction is reversed, the shape becomes its mirror image so the E-field rotation changes its helicity which flips the out-of-plane T-spin. This new T-spin provides an additional degree of freedom for excitation of the CSW which can be directionally excited by an in-plane CP source as well as an out-of-plane CP source.

4.3 Experimental Results

The measured results of the L-shape metasurface is presented in Fig. 4.5. The L-shape surface is fabricated on a printed circuit board of Rogers 5880 ($\varepsilon_r = 2.2$) which results in a shift in the frequency of the supported CSW from 17.5 GHz to 14.5 GHz. Fig. 4.5(b) and 4.5(c) show the magnitude of the E_z normalized by the maximum value in the units (V/m). The directional excitation is observed for the L-shape surface when excited with circularly polarized dipole sources of opposite helicities at the center. The surface is excited with two probe antennae oriented along x and y directions where the magnitude and phase of E_z are measured for each probe excitation separately. The measured magnitudes and phases are then added with a phase shift of 90 degrees to form an excitation of $\mathbf{E}_x \pm i\mathbf{E}_y$ as depicted in the following equation:

$$\mathbf{E}_z^x \pm i\mathbf{E}_z^y = |\mathbf{E}_z^x| \cos\left(\phi_z^x\right) + |\mathbf{E}_z^y| \cos\left(\phi_z^y \pm 90^0\right), \tag{4.8}$$

where $\mathbf{E}_z^{x(y)}$ is the measured $\mathbf{E}_z$ when excited with a probe along $x(y)$-axis. Using the 45^0 mirror symmetry of the L-shape surface, an excitation with an x-probe along the vertical arm of the L-shape can be mirrored to a y-probe excitation along its horizontal arm. Since the excited mode is propagating along the diagonal of the surface, $\mathbf{E}_z^y$ can be extracted from $\mathbf{E}_z^x$ by flipping the vector across the normal to the diagonal of the surface or by simply rotating the measured E-field vector by 180 degrees. A detailed discussion on the forward to backward ratio for the measured E-field can be found in the Supplementary Information Section.

4.4 Conclusion

We have shown numerically and experimentally the possibility of the excitation of a new type of surface wave called a chiral surface wave which unlike other surface waves, possesses two transverse spins, an in-plane transverse spin that is inherent to any surface wave and an out-of-

plane transverse spin that is enforced by the L-shape design. We showed that due to the 45^0 mirror symmetry and the broken rotational symmetry of the L-shape design, it results in strong in-plane E-field rotation and spin splitting in k-space. The two transverse spins follow the spin-momentum locking law resulting in spin-dependent directional propagation. Another important feature of the L-shape design is that it has flat EFC which results in a highly collimated surface wave. This work provides a new degree of freedom for controlling the spin-orbit interaction of evanescent waves by adding an extra transverse spin. This additional degree of freedom expands our understanding of the spin-momentum locking law which has been extensively studied before but for only one transverse spin. We show that supporting highly collimated spin-dependent unidirectional modes with strong spin-orbit interaction can be done using a homogeneous metasurface design without the complexity of designing bandgap materials or interfaces between different materials.

This chapter is based on *Chiral surface wave propagation with anomalous spin-momentum locking* by S. Kandil, D. Bisharat and D. Sievenpiper, *ACS Photonics*. The dissertation author was the primary author of this material.

4.5 Supplementary Information

4.5.1 Definition of different terminologies

Mirror Inversion symmetry: when a shape reproduces itself after being reflected by a mirror plane.

Rotational symmetry: when a shape reproduces itself after being rotated less than one full turn. It is denoted by C_n where n is the number of times it reproduces itself during a 360-degree rotation. C_1 means it has broken rotational symmetry. By default, the axis of rotation is the z-axis unless it is stated in the subscript otherwise, e.g.: C_{2x}.

Polarizability: an expression of the tendency of a shape to acquire an electric/magnetic dipole moment when subjected to an external electric field. It can be expressed in terms of the dipole

moments and incident E- and H-fields as follows:

$$\mathbf{p} = \overline{\overline{\alpha}}_{\mathrm{ee}}.\mathbf{E}_{\mathrm{inc}} + \overline{\overline{\alpha}}_{\mathrm{em}}.\mathbf{H}_{\mathrm{inc}}, \tag{4.9}$$

$$\begin{bmatrix} p_x \\ p_y \end{bmatrix} = \begin{bmatrix} -\alpha_{ee}^{xx} & -\alpha_{ee}^{xy} \\ -\alpha_{ee}^{yx} & -\alpha_{ee}^{yy} \end{bmatrix} \begin{bmatrix} E_{inc_x} \\ E_{inc_y} \end{bmatrix} + \begin{bmatrix} -\alpha_{em}^{xx} & -\alpha_{em}^{xy} \\ -\alpha_{em}^{yx} & -\alpha_{em}^{yy} \end{bmatrix} \begin{bmatrix} H_{inc_x} \\ H_{inc_y} \end{bmatrix} \tag{4.10}$$

The electric polarizability, $\overline{\overline{\alpha}}_e e$, has the units of: $C.m^2/V$. The electromagnetic polarizability, $\overline{\overline{\alpha}}_e m$, has the units of: $C.m^2/A$ or $m^2 s$.

Chirality of a shape: a shape is considered chiral if its mirror image cannot be superimposed on itself even after rotation and/or translation. A shape is said to be chiral if it possesses this feature in all possible mirror planes in the three dimensions. However, in-plane chirality is demonstrated for structures that are not superimposable with their mirror images except for when the mirror plane is parallel to its surface.

Chirality of a surface wave: a surface wave is considered chiral if it possesses a circularly polarized electric or magnetic field whose spin direction (normal to the plane of the field rotation) is in the transverse direction, and it obeys the spin-momentum locking law which states that the transverse spin direction should be normal to the momentum direction. This means that if the helicity of the circular polarization is reversed, the wave propagates in the opposite direction. There are two transverse spins for any chiral surface wave that is collimated (with single propagation direction) which are in-plane and out-of-plane transverse spins.

4.5.2 More on Self-Collimation

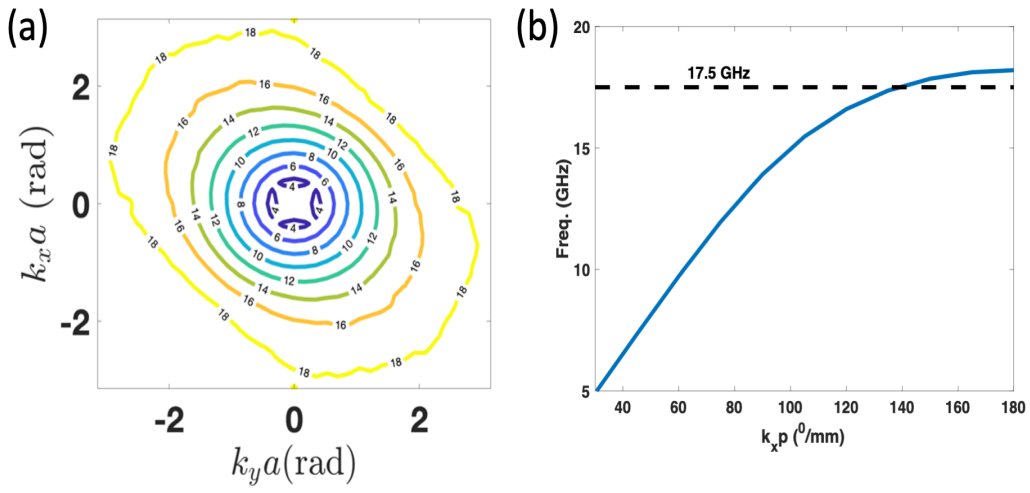

Figure 4.6: (a)The EFC of the L-shape unit cell (b) and its dispersion diagram

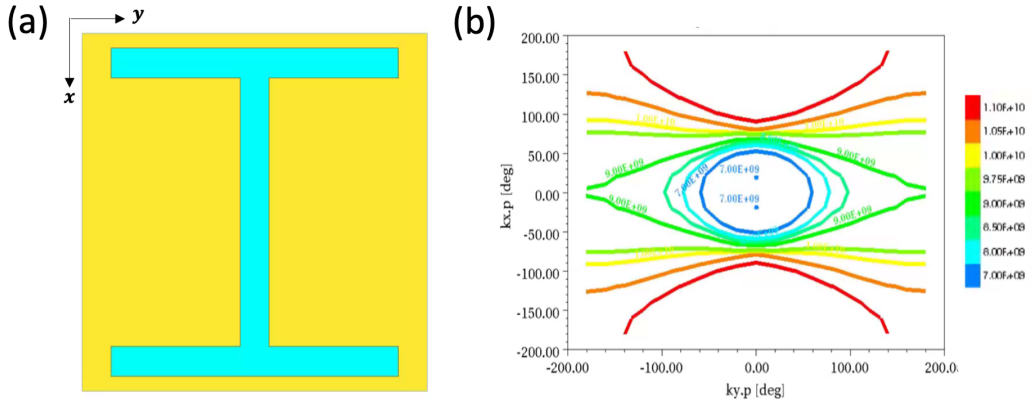

Figure 4.7: (a) The unit cell of the I-shaped hyperbolic metasurface and (b) its EFC.

Using the calculated EFCs, the direction of propagation for the supported interface mode at different frequencies can be determined. The EFC of the L-shape is shown in Fig. 4.6(a), where it can be demonstrated that the $\pm\pi/4$ direction is the only allowed propagation direction

for the supported surface wave which has the outermost yellow contour at around 17.5 GHz. The dispersion diagram shown in Fig. 4.6(b) depicts that the frequency of operation of the surface wave is around 17.5 GHz. At lower frequencies, the surface wave becomes less confined to the interface.

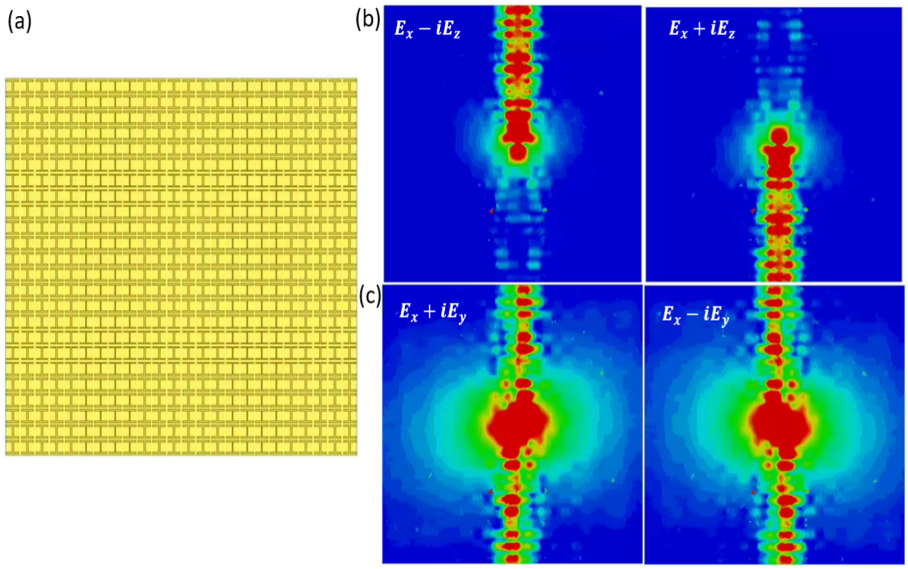

Figure 4.8: (a) The hyperbolic I-shaped metasurface. The simulated E-field plots when excited with (b) an in-plane T-spin ($E_x \pm iE_z$) and (c) an out-of-plane T-spin ($E_x \pm iE_y$).

High self-collimation by itself is not enough to have an out-of-plane T-spin. The shape must have the symmetry properties discussed in the Chapter. An example is the I-shaped hyperbolic metasurface [2] which supports highly self-collimated surface waves but doesn't possess an out of plane T-spin. It can be shown from the EFC that at 9.75 GHz, the hyperbolic design has a flat contour. The simulated E-field plots in Fig. 4.8 show that it achieves spin-momentum locking when excited with an in-plane T-spin ($E_x \pm iE_z$) while it propagates in both directions when excited with an out-of-plane T-spin ($E_x \pm iE_y$). This concludes that the I-shape doesn't support an out-of-plane T-spin.

4.5.3 Comparison between the L-shape and other shapes

As stated in this Chapter, the L-shape has two important features that make it efficient for supporting a chiral surface wave which are: (1) having 45^0 mirror inversion symmetry which allows for orthogonal mode coupling, this is represented by strong α_{ee}^{xy} and (2) broken rotational symmetry and this results in splitting the spin in k-space. Different variations of the L-shape and their symmetry properties are discussed here. By shifting the vertical slit in the L-shape towards the center, two effects take place: (1) the 45^0 mirror inversion symmetry decreases resulting in a lower α_{ee}^{xy} due to the smaller overlapping area between the shape and its mirror image which reaches zero for the T-shape. This is shown in Fig. 6. (2) The asymmetry of the shape along the x- and y- axis results in different magnitudes of the α_{ee} diagonal elements.

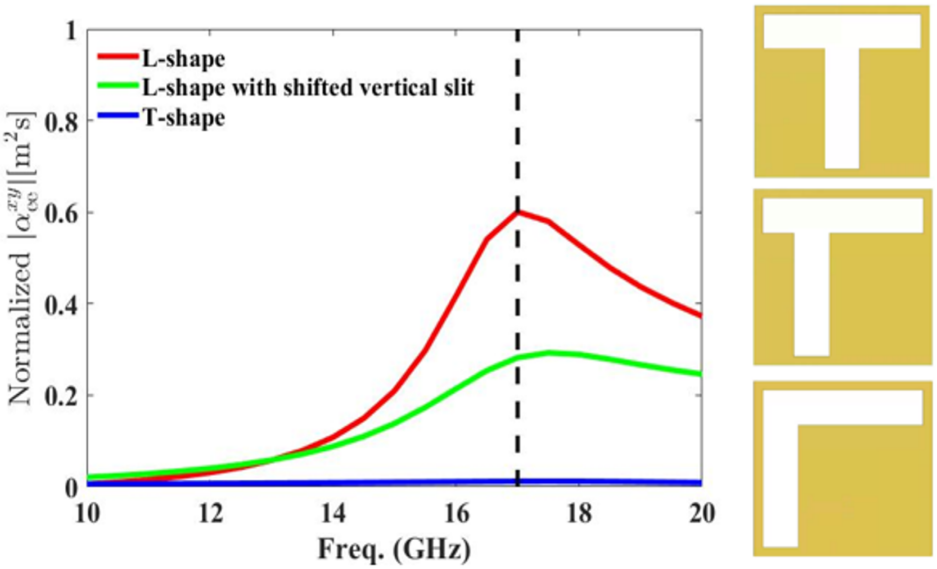

Figure 4.9: Normalized α_{ee}^{xy} comparison between the L-shape, T-shape and L-shape with shifted vertical slit.

Different shapes, their symmetry, chirality, and polarizability tensors are shown for illustration in the schematic shown in Fig. 7. It is important to emphasize that the chirality of the shape is not necessarily correlated to its ability to support chiral surface wave. The shape must also possess strong x-to-y coupling and broken rotational symmetry. Shapes with only C_{2x} or

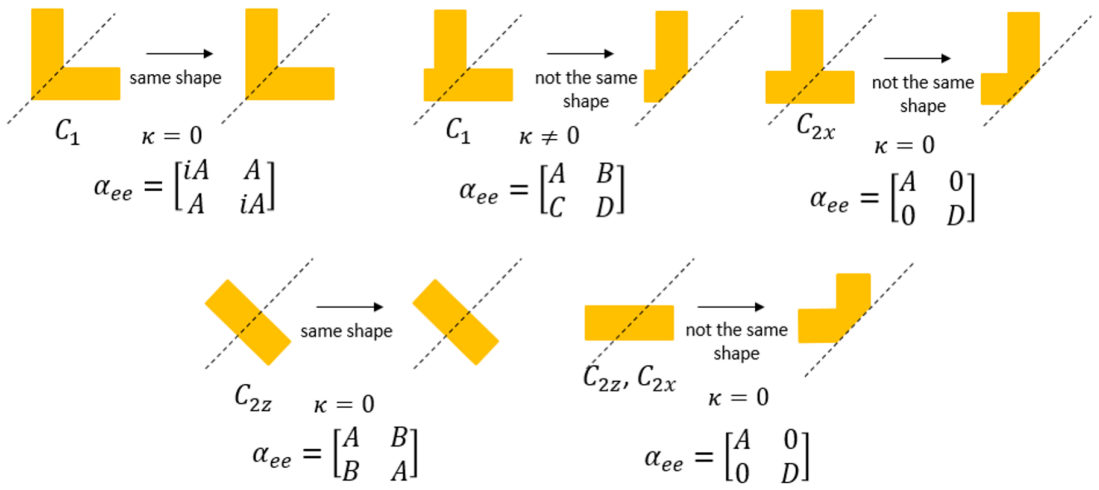

Figure 4.10: Comparison of the α_{ee} tensor for different shapes highlighting their rotational symmetry and chirality parameter.

only C_{2y} will have asymmetry along the x- and y-axis which results in having different diagonal elements (x-to-x y-to-y). Shapes with 45^0 mirror inversion symmetry as well as rotational symmetry of C_{Nz} where N2 will have nonzero x-to-y coupling, but different x-to-x and x-to-y coupling terms. Table 1 summarizes some of the key conclusions.

It is important to note here that the 45^0 mirror inversion symmetry results in a non-zero x-to-y coupling but is not sufficient for achieving a chiral surface wave. An example of that is the vertical slit rotated by 45^0. Additionally, not having a 45^0 mirror inversion symmetry does not always result in a zero x-to-y coupling term. An example for that is the L-shape with shifted vertical slit (middle top of Fig. 4.10) which still have a small x-to-y coupling (this case is not included in the table).

4.5.4 Demonstration of the phase shift between E-field components of each T-spin

An out-of-plane transverse spin means that the E-field is rotating in plane. This corresponds to 900 phase shift between E_x and E_y where both have the same magnitude for an ideal

circularly polarized rotation as the case in the L-shape metasurface discussed in this work. The 900 phase shift as well as the different spin strengths of both T-spins can be deduced and explained through the following analysis: Fig.4.11(a) shows the magnitudes of $E_{x'}$ and $E_{y'}$ (for S_z) and the magnitudes of $E_{x'}$ and E_z (for $S_{x'}$) are shown in Fig.4.11(c) where the differences between their phases are shown in Fig.4.11(b) and Fig.4.11(d); all quantities are calculated along the diagonal line of the metasurface where the CSW propagates when excited with a linearly polarized dipole source at the center (at approximately a distance=75mm). The modified coordinates x', y' are x,y rotated by 45^0 in clockwise direction as depicted in Fig. 4.3(a). It can be observed that $E_{x'}$ and $E_{y'}$ are almost equal in magnitude (the mean value of $\|E_{x'}$ - $E_{y'}\| \approx 0$) and their phase shift is 270^0 (equivalent to -90^0) along the forward propagation direction which changes to -270^0 (equivalent to $+90^0$) at the backward propagation direction. Similarly, it can be depicted that E_z is higher in magnitude than $E_{x'}$ (the mean value of $\|E_z$ - $E_{x'}\| > 0$) and their phase shift changes from $+90^0$ along the forward direction to -90^0 along the backward direction. The high E-field peaks at the center are due to the excitation dipole source.

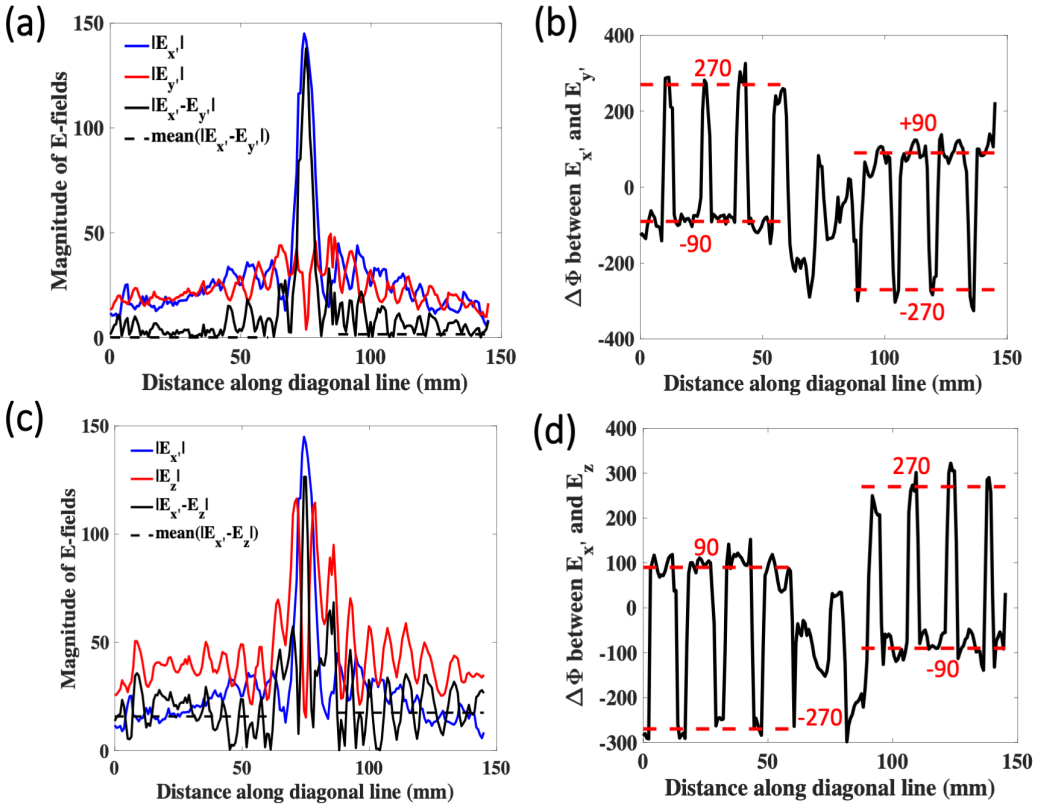

Figure 4.11: (a) Magnitudes of $E_{x'}$ and $E_{y'}$ and the mean value of the difference between them as well as (b) their phase shift in degrees. (c) Magnitudes of $E_{x'}$ and E_z and the mean value of the difference between them as well as (b) their phase shift in degrees.

In a simpler format, the ellipticity can be used to evaluate the ratio between the two axes of the field rotation for each spin state. It is calculated for the two transverse spins using the following equations:

$$\varepsilon_{y'} = \frac{E_{x'}}{E_z} \tag{4.11}$$

$$\varepsilon_z = \frac{E_{x'}}{E_{y'}} \tag{4.12}$$

where as depicted in Fig. 4.12, $\varepsilon_z = 0.97$ and $\varepsilon_{y'} = 0.52$.

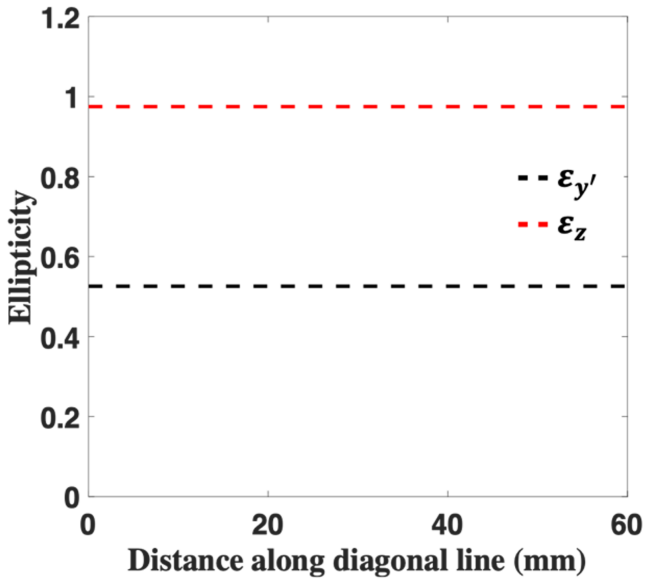

Figure 4.12: The ellipticity calculated from the simulated E-fields for the two T-spins, S_z and $S_{y'}$.

According to the above discussion, it can be deduced that $E_{x'}$ and $E_{y'}$ form an ideal circular polarization while $E_{x'}$ and E_z form an elliptical polarization with ellipticity of 0.52. Hence, the three E-field components can be approximately written as follows:

$$E_{y'} = \|E\|, \quad E_{x'} = \|E\|e^{-i\frac{\pi}{2}}, \textit{and} \quad E_z = 2\|E\|e^{-i\pi} \tag{4.13}$$

By calculating the electric spin density as defined in 4.1, we can find the spin densities normalized by the electric energy ($\|\mathbf{E}\|^2 \approx 6\|E\|^2$) to be:

$$S_{x'} = \frac{\mathrm{Im}\left\{E_{x'}E_{y'}^* + E_{x'}^*E_{y'}\right\}}{6\|E\|^2}. \tag{4.14}$$

$$S_{y'} = \frac{\mathrm{Im}\left\{-E_{x'}E_z^* + E_{x'}^*E_z\right\}}{6\|E\|^2}, \tag{4.15}$$

$$S_z = \frac{\mathrm{Im}\left\{E_{x'}E_{y'}^* + E_{x'}^* E_{y'}\right\}}{6\|E\|^2}. \tag{4.16}$$

By substituting with $E_{x'}$, $E_{y'}$ and E_z expressions in terms of $\|E\|$, the values of the three spin components can be found as follows:

$$S_{x'} = 0, \quad S_{y'} = \frac{2}{3}, \; and \quad S_z = \frac{1}{3}. \tag{4.17}$$

These values match the values extracted from the HFSS simulation shown in Fig. 4.13. The total spin density is 1 where the strengths is distributed between the two T-spins: S_z and $S_{y'}$.

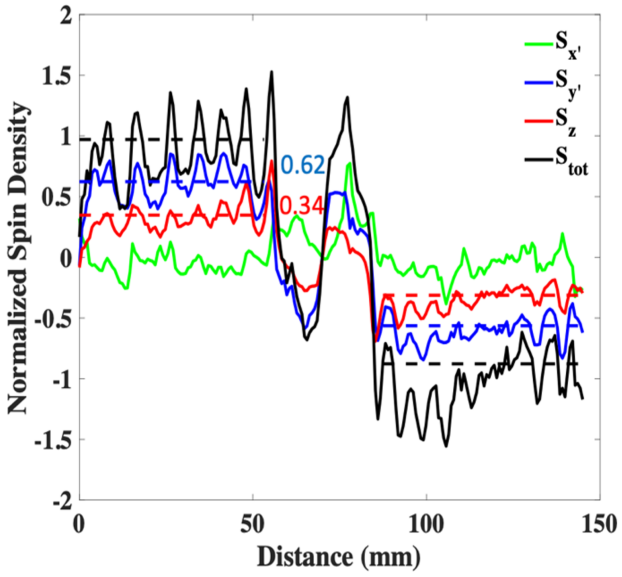

Figure 4.13: The normalized spin densities along x',y' and z directions where the total Spin density (sum of all three) is shown in black. The dotted lines show the mean value for each of the spin densities.

The propagation of chiral SW (with anomalous T-spin) relies on satisfying the symmetry condition for achieving the in-plane E-field rotation as explained in Eq. 4.5. By inspecting the $\|\alpha_{ee}^{xy}\|$ for the L-shape at different frequencies shown in Fig. 4.2 in the manuscript, it can be

concluded that the L-shape has a resonant behavior where the condition is satisfied and has the optimum results at 17.5GHz.

By simulating the E-field when excited with the in-plane CP dipole source at different frequencies, it can be shown in Fig. 4.14 that the 3dB bandwidth calculated from the directionality ratio (defined as the ratio between the forward and backward propagating field powers) is approximately from 16.5 GHz to 17.7 GHz. This means it has an operation bandwidth of around 1.2GHz which means it is not a broadband device.

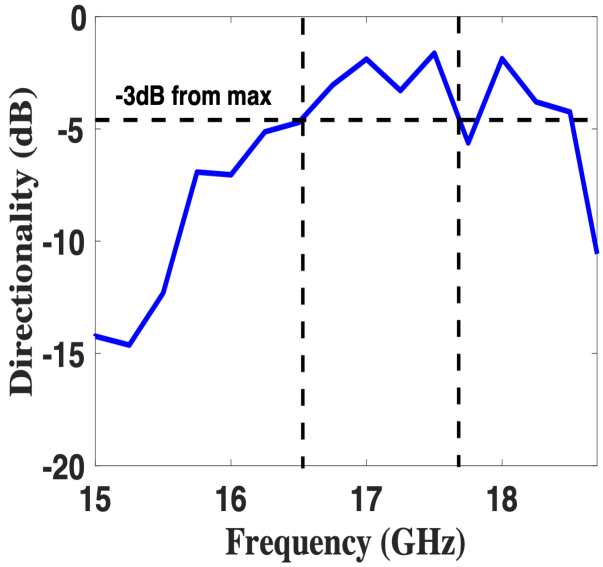

Figure 4.14: The directionality ratio defined as the ratio between the forward and backward field powers in dB calculated from the full surface field simulations when excited with an in-plane CP dipole source.

Chapter 5

3D Photonic Crystal for Spin-dependent Propagation

5.1 Introduction

In the previous chapters, we studied 1D waveguide and 2D metasurface designs to achieve high spin-dependent directional surface wave propagation. We showed that the common idea behind enhancing and controlling the spin properties of the surface waves is by engineering the symmetry of the design itself. This includes breaking the rotational symmetry as in the L-shape and the C-shape where the broken rotational symmetry results in flatter EFCs and spin-splitting in the k-space. In this Chapter, we will study spin-dependent propagation in 3D photonic crystals. Similar to 1D and 2D designs, in 3D structures, the broken inversion symmetry of the whole design can result in enhanced spin-orbit coupling. This was first demonstrated in Dresselhaus systems which inherently have low symmetry [82], and Rashba systems where the material is cut at a certain interface [83].

Breaking the inversion symmetry in 3D crystals can be induced by line defects [84–86]. Historically, defects were considered a nuisance in semiconductors which abrupt its electrical

and structural properties [85, 87]. However, they have been recently shown to induce inversion symmetry breaking resulting in strong spin-orbit coupling [88–91]. It was demonstrated that dislocations in crystals can result in topologically protected states [88]. A large spin-splitting was observed in the defect states of Se vacancy line defects placed in monolayer transition metal dichalcogenide (TMD) [91]. Additionally, placing two parallel chalcogen vacancy line in monolayer TMDs has shown to result in a unidirectional spin-orbit interaction [89]. There are various types of line defects; the most common ones are edge, screw and mixed. A screw dislocation can be visualized as the crystal being split into two halves at its center where one half is sheared away from the other by one lattice constant or multiples of it. This dislocation creates a helical arrangement of the atoms/spheres normal to the direction of the stress which forms a helicoidal field. Screw dislocations have been studied in 3D acoustic topological insulators where dislocation-induced robust helical modes were observed [92]. It was also tested in photonic topological insulators by stacking 2D ring resonator lattices with a synthetic frequency dimension where one-way transport of photons was observed after placing the screw dislocation [93]. Additionally, one-way modes were demonstrated in 3D magnetic Weyl photonic crystal when the supercell modulation takes a helical form [94].

For implementing the screw dislocation in 3D photonic systems, we need a 3D photonic crystal that experiences a complete bandgap in the three dimensions. 3D photonic crystals are arrays of dielectric spheres that can take different lattice configurations from cubic, HCP, BCC, FCC and Diamond [95]. It was first demonstrated in [96] that the diamond lattice possesses a complete 3D photonic bandgap when the radius of the spheres is large enough that they overlap. This makes the Diamond crystal lattice a suitable 3D photonic structure for screw dislocation.

In this Chapter, we will investigate the Diamond photonic crystal and its band structure. We will show we can produce a localized mode in the bandgap of the 3D diamond photonic crystal by introducing a screw dislocation defect along the center of the crystal. We will also study the spin properties of this localized mode and show it has spin-dependent directionality

properties.

5.2 Diamond Photonic Crystal

Fig. 5.1(a), (b) and (c) show the cubic supercell, rhombohedral primitive cell and the inverse opal of the primitive cell of the Diamond photonic crystal, respectively. As shown, the diamond lattice consists of dielectric spheres with $\varepsilon_r = 10$ and radius $= 0.2405a$, where a is the lattice constant of the cubic supercell. The rhombohedral primitive cell is the smallest possible unit cell which contains one lattice symmetry while the cubic (conventional) supercell contains the full symmetry. The primitive cell can be used to simplify the simulation for calculating the band diagram of the diamond photonic crystal. It has been shown in the literature that the Diamond photonic crystal composed of dielectric spheres in air environment as well as its inverse opal which is composed of air spherers in a dielectric envelope possess the 3D photonic bandgap. For simplicity of fabrication, we decided to study the inverse opal structure.

The primitive lattice vectors for the diamond lattice are defined as follows:

$$\vec{\mathbf{a}}_1 = \frac{a}{2}(\vec{\mathbf{y}} + \vec{\mathbf{z}}), \tag{5.1}$$

$$\vec{\mathbf{a}}_2 = \frac{a}{2}(\vec{\mathbf{x}} + \vec{\mathbf{z}}), \tag{5.2}$$

$$\vec{\mathbf{a}}_3 = \frac{a}{2}(\vec{\mathbf{x}} + \vec{\mathbf{y}}). \tag{5.3}$$

while the three primitive reciprocal lattice vectors are defined as:

$$\vec{\mathbf{b}}_1 = \frac{2\pi}{V}(\vec{\mathbf{a}}_2 \times \vec{\mathbf{a}}_3), \tag{5.4}$$

$$\vec{\mathbf{b}}_2 = \frac{2\pi}{V}(\vec{\mathbf{a}}_1 \times \vec{\mathbf{a}}_3), \tag{5.5}$$

$$\vec{\mathbf{b}}_3 = \frac{2\pi}{V}(\vec{\mathbf{a}}_1 \times \vec{\mathbf{a}}_2). \tag{5.6}$$

where V is the scalar triple product of the primitive lattice vectors. The wave vector $\vec{k}$ can be written in terms of the reciprocal lattice vectors as:

$$\vec{\mathbf{k}} = u\vec{\mathbf{b}}_1 + v\vec{\mathbf{b}}_2 + w\vec{\mathbf{b}}_3. \tag{5.7}$$

where u, v, and w are the three reciprocal lattice vector constants varying for each symmetry point. Thus, the 3D band diagram of the first Brillouin zone can be numerically calculated using Eq.5.7 which is shown in Fig. 5.1(d). It can be observed that a 3D bandgap is produced at frequencies 11.9GHZ to 13.7GHz.

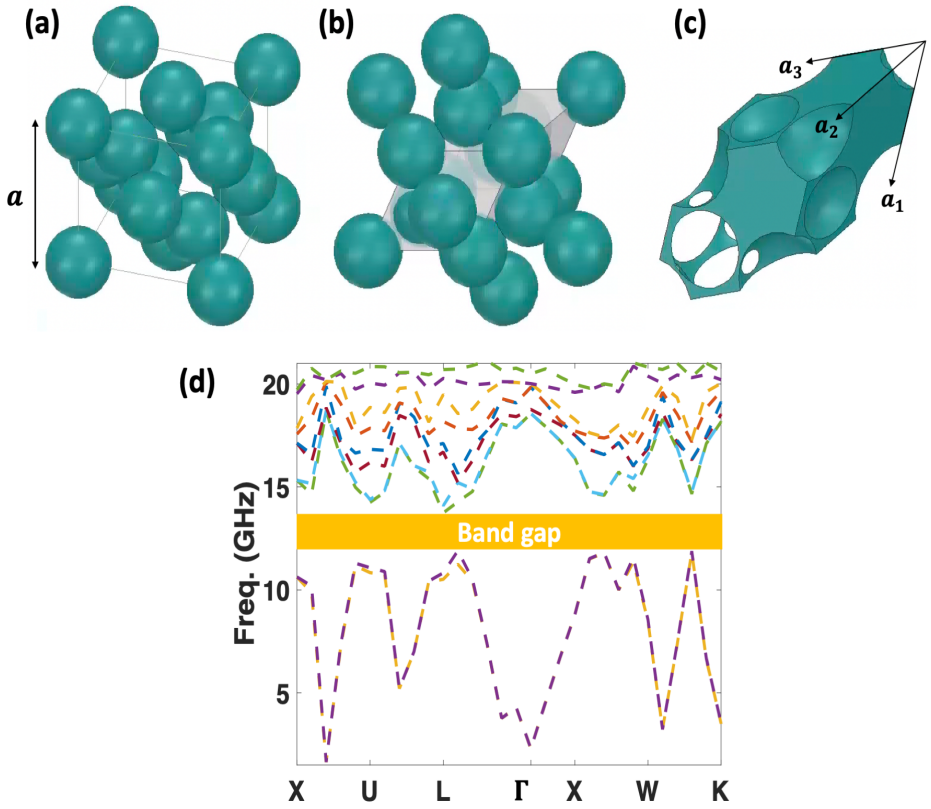

Figure 5.1: (a) Cubic unit cell of diamond photonic crystal composed of dielectric spheres. (b) The rhombohedral primitive unit cell is highlighted. (c) Inverse opal of the primitive unit cell of diamond photonic crystal. (d) The band diagram calculated numerically where the bandgap is highlighted in yellow.

5.3 Screw Dislocation in Diamond Photonic Crystal

5.3.1 Design and Mode study

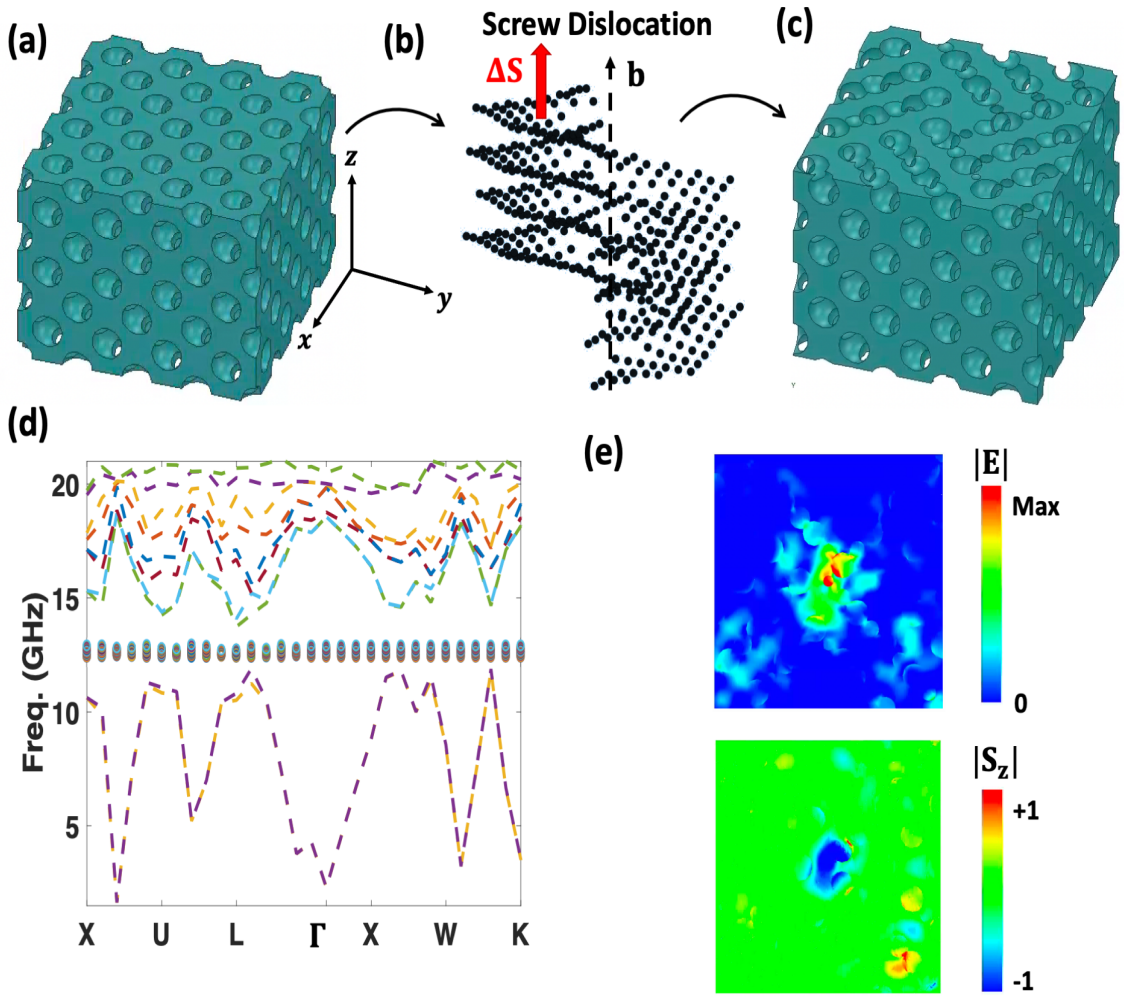

Figure 5.2: (a) Inverse opal diamond photonic crystal without dislocation. (b) Schematic demonstrating the screw dislocation in a diamond crystal made of dielectric spheres. The Burgers vector, **b** is shown. (c) The inverse opal diamond crystal after implementing the screw dislocation. (d) The band diagram of the diamond crystal where the new modes induced after implementing the screw dislocation are shown in the bandgap. (e) Magnitude of E-field map for the localized mode found in the bandgap (top) and magnitude of spin density vector in the z-direction (bottom); both numerically calculated using the Eigenmode simulation.

We then introduce the screw dislocation in the diamond lattice. Fig. 5.2(b) shows a schematic of the screw dislocation in the crystal. A burgers vector, **b**, expresses the magnitude

and direction of the distortion to the lattice. In screw dislocation, **b** is parallel to the shear direction which is here along the z-axis. **b** here is taken as $0.5a$. The shift along the z-axis is defined as: $\Delta\mathbf{S} = \theta\mathbf{b}/2\pi$, where θ is the angle between the sphere center and the z-axis (defined from the polar coordinates of the sphere location).

Fig. 5.2(a) and (c) show the diamond crystal before and after introducing the screw dislocation, respectively. The band diagram calculated for the supercell as presented in Fig. 5.2(d) show modes form in the bandgap of the diamond lattice. The calculated the E-field map of one of the modes formed in the bandgap clearly shows a localized mode at the center of the lattice as presented in Fig. 5.2(e), top. By calculating the spin density of this localized mode using Eq. 1.3, as shown in Fig. 5.2(e), bottom, the mode is found to possess field rotation in the x-y plane resulting in non zero S_z. The frequency at which the localized is found to exist is 12.2GHz. Other modes found in the bandgap correspond to corner states and artificial boundary effects.

5.3.2 Results

Now, that we confirmed the presence of a localized mode that is spin-polarized in the diamond lattice after introducing the screw dislocation, here we study the transmission properties of this mode. Fig. 5.3(a) presents a comparison between the magnitude of the E-field maps calculated at the y-z plane cross-section for the diamond lattice before (left) and after (right) introducing the screw dislocation at 12.2GHz. The lattices are excited from the top center with a CP dipole defined as: $E_x + iE_y$. As observed, a high transmission of the wave at the bandgap frequency in the screw dislocation while no transmission for the diamond lattice. Fig. 5.3(b) presents the magnitude of E calculated at 12.2GHz along a line in the z-direction along the center of the lattice which shows the large difference in magnitudes for the diamond lattice with and without the dislocation. In Fig. 5.3(c), we study the E-field intensity at different frequencies by calculating the sum of the magnitude of E-field along the center line at different frequencies for the diamond lattice with and without the screw dislocation. There is a clear peak in the E-field

intensity for the screw dislocated lattice at 12.2GHz while a low E-field intensity is found at bandgap frequencies for the pure diamond lattice (without dislocation).

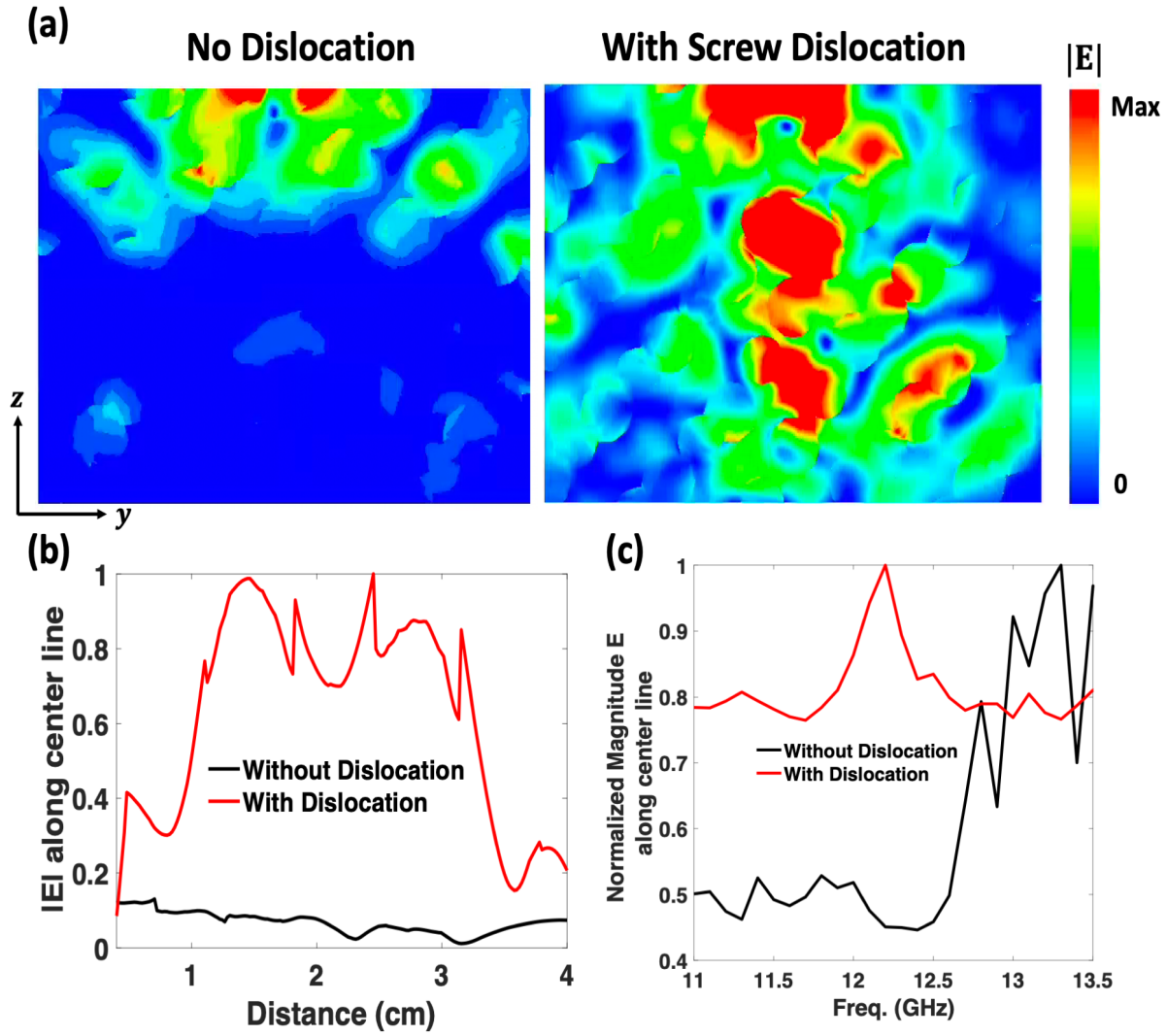

Figure 5.3: (a) Magnitude of E-field map for Diamond photonic crystal without screw dislocation (left) and with screw dislocation (right) in the y-z plane. (b) 2D plot for the magnitude of E-field calculated along a line at the center of the diamond crystal. (c) Normalized magnitude of the sum of the E-field along the center of the crystal calculated numerically at different frequencies.

5.3.3 Spin-dependent Wave Propagation

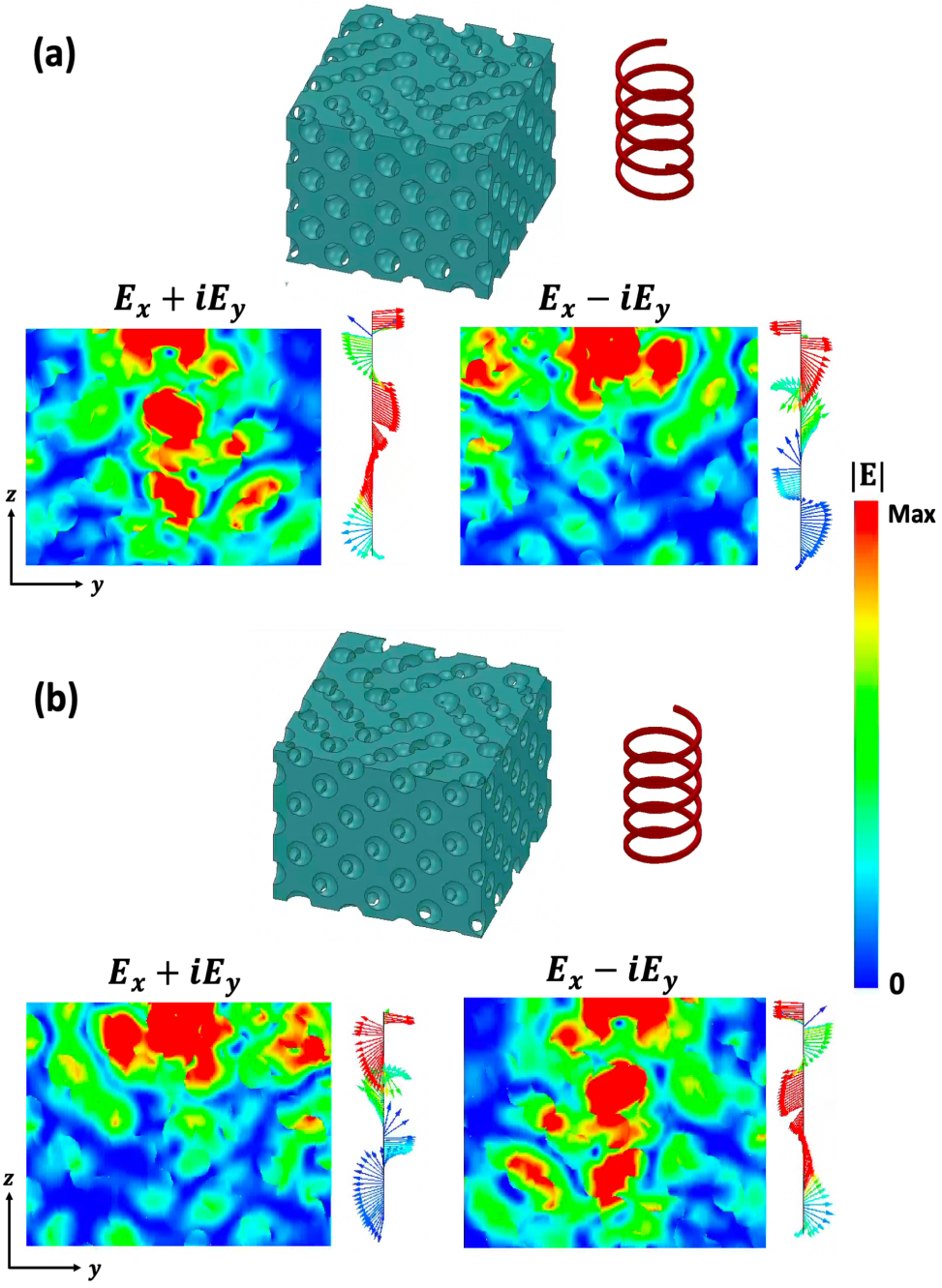

Figure 5.4: (a) Screw dislocation in Diamond photonic crystal with anticlockwise screw helicity. The magnitude of E-field maps are shown in the y-z plane when the crystal is excited with $E_x + iE_y$ and $E_x - iE_y$. (a) Screw dislocation in Diamond photonic crystal with clockwise screw helicity. The magnitude of E-field maps are shown in the y-z plane when the crystal is excited with $E_x + iE_y$ and $E_x - iE_y$.

To further demonstrate the spin-dependent directionality of the diamond lattice with the screw dislocation, we monitor the wave transmission when opposite helicities of the CP dipole sources are used to excite the lattice as well as when the helicity of the screw dislocation itself in the lattice is flipped.

In Fig. 5.4(a), the E-field maps for the diamond lattice with a clockwise screw dislocation are shown; a helix is shown on the right to illustrate the helicity of the screw. It can observed that the wave propagates when the excitation CP dipole source has a helicity that matches the helicity of the screw dislocation while the opposite helicity is blocked. This is confirmed when studying the diamond lattice with an anti-clockwise screw dislocation shown in Fig. 5.4(b). The wave propagates when excited with an $E_x - iE_y$ source which matches the anti-clockwise screw helicity.

5.4 Conclusion

In this Chapter, we demonstrated that introducing a screw dislocation in a diamond photonic crystal results in forming a mode in the bandgap that is localized at the center of the lattice. We also studied the spin-dependent properties of the induced mode and showed it is spin-polarized where the direction of the spin vector is matches the helicity of the screw dislocation. This work provides a 3D waveguide that produces spin-polarized unidirectional wave propagation which can be used in lots of applications such as quantum information processing and sensing.

This chapter is based on *Screw Dislocation in Diamond Photonic Crystal for Spin-dependent Propagation* by S. Kandil, Y. Zhou, P. R. Bandaru and D. F. Sievenpiper, *In preparation*. The dissertation author was the primary author of this material.

Chapter 6

Conclusion

6.1 Summary and Applications

Over the last decade, much research has been directed towards designing metasurfaces that can control the wave propagation. In this thesis, we demonstrated numerically and experimentally different designs in 1D, 2D and 3D structures where spin-dependent wave propagation is achieved. We demonstrated the capability to control the propagation of surface waves based on their spin direction by engineering the symmetry of the design. We have explored different types of method to enhance the spin-dependent directionality whihc can be summarized in the following: 1) symmetric dipole-dipole coupling in multimode composite unit cell, 2) engineering equifrequency contours and increasing self-collimation through broken rotational symmetry, 3) designs with 45^0 mirror symmetry for chiral surface waves with two T-spins, and 4) breaking internal inversion symmetry in 3D photonic crystals by introducing screw dislocations. Our study provides a new direction for enhancing and controlling the spin-properties of electromagnetic waves by engineering the symmetry of the design.

In Chapter 2, we presented a 1D waveguide design composed of three C-shaped metallic structures where the dipole to dipole coupling between the adjacent metallic cells was shown

to play a role in controlling the spin density. Numerical simulations showed spin-dependent unidirectional propagation was supported where a directionality ratio of 95% was reached. Additionally, a robustness study against different defects was implemented showing the directionality of the chiral waveguide is sensitive to defect at the center and defects that flip the spin of the wave.

A 2D metasurface version of the C-shape waveguide is presented in Chapter 3. In this Chapter we demonstrated how engineering the EFC can result in highly collimated surface wave propagation where various wave properties are achieved at different frequency contours. By adjusting the frequency, the wave can be split into two waves with opposite spins where the split angle increases as the frequency increases. Additionally, by rotating the unit cells, we showed numerically and experimentally the surface wave can be steered along a specified curved path.

In Chapter 4, we introduced a new type of surface waves called chiral surface waves that is supported by an L-shaped metasurface. Chiral surface waves, unlike other surface waves, possess two transverse spin due to out-of-plane and in-plane field rotation. We analyzed the symmetry properties of the shape and showed its broken rotational symmetry as well as 45^0 mirror symmetry result in its additional T-spin. The spin density study showed the two T-spins are locked to the momentum resulting in spin-dependent directional wave propagation.

Chapter 5 demonstrated the spin-dependent propagation achieved in 3D photonic crystals by breaking the internal inversion symmetry through introducing screw dislocation. The diamond photonic crystal was used in this study for its complete 3D bandgap. Breaking the lattice symmetry with the screw dislocation resulted in spin-polarized localized mode inside the bandgap at the center of the lattice.

Spin-dependent wave propagation achieved on flat surfaces and waveguides give them the advantage of being easily integrated to photonic devices for flat optics approach. The devices explored in this thesis can be used in surface waveguiding due to their high self-collimation and polarization-based beam splitters. Additionally, their spin properties can play an important role

in quantum information processing, sensing and spin filtering. Until recently phenomena such as spin-hall effect was thought to only exist in complicated topological designs and bandgap materials. Exploring the capabilities that can be reached using simple designs by engineering their symmetry deepens our understanding of Maxwell's equations and the spin-orbit interaction of electromagnetic waves.

6.2 Potential Future Work

In Chapter 4, we presented the L-shaped metasurface that possesses two T-spins. An example of future work is to perform robustness study on metasurfaces that possess two T-spins versus ordinary one that possess one T-spin by placing different types of defects and calculating the backscattering. This will contribute to the understanding of chiral surface waves behaviors and properties. Also, it will help quantify the spin-orbit interaction associated with different surface waves. The following figure shows a preliminary simulations done to test how bending the surface can affect the chiral SW propagations. The E-field distribution plots show minimal backscattering.

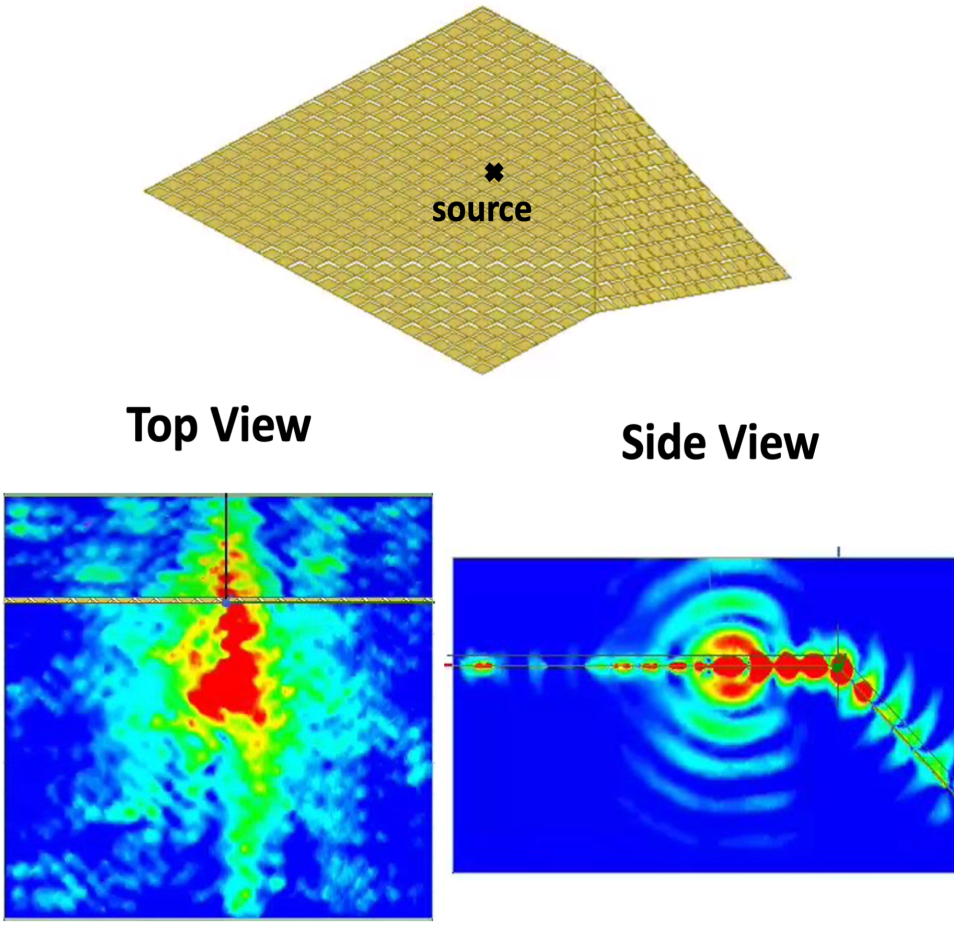

Figure 6.1: Bending L-shape metasurface.

In Chapter 3, we discussed engineering the EFC to enforce certain propagation direction. Additional ways to do that can be done through stacking different metasurface designs where dipole-dipole interaction can take place between stacked layers and result in modifying the EFCs. This is sometimes termed as Moire surfaces. In the figure below, we show how stacking L-shape design with itself but rotated by 90 degrees can change its EFC shape. Similarly, the same stacking mechanism was performed on the omega-shape.

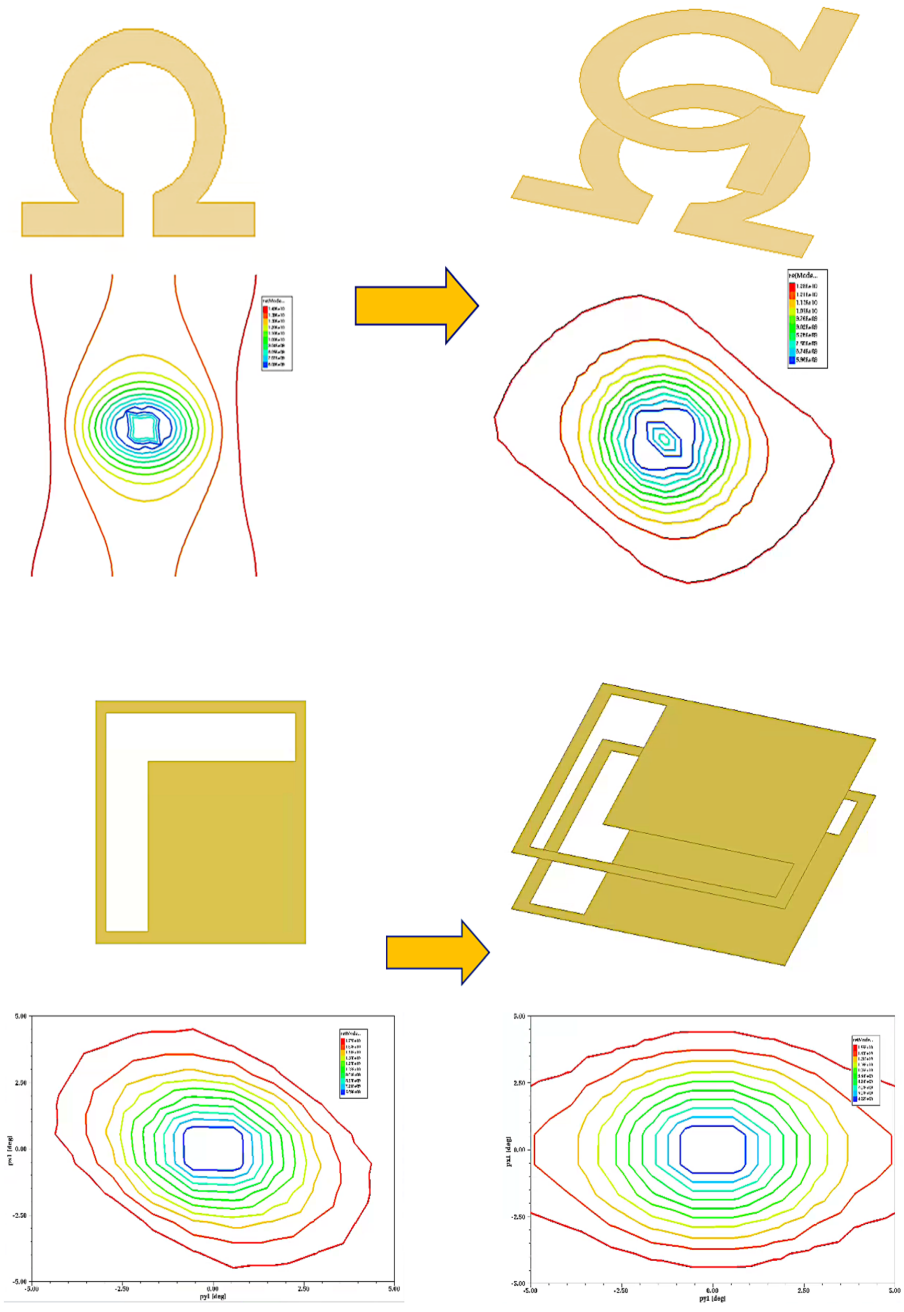

Figure 6.2: Stacked metasurfaces for engineering EFCs.

Other potential future work include integrating spin-based photonic devices to spin-based electronic devices which can result in faster, scalable, and more controlled electron-photon interactions. Although these two systems are usually studied separately, emerging research areas

require the two systems combined. For example, in [97], the authors demonstrated a device that integrates between an electronic topological insulator which achieves directional, spin-polarized photocurrent in a Bi_2Se_3 layer with a photonic waveguide. They were able to show the strong interaction between the guided light wave and directional electrons where changing the light propagation direction reverses the electron spin and vice versa. These integrated platforms can provide an additional degree of freedom to control the spin of the electron and/or the photon as well as transmission robustness. Besides, they can enhance spin-orbit coupling for lots of applications in quantum information processing.

Another example for possible applications to the electron-photon integrated systems is related to the orbital angular momentum (OAM) control as presented in [98] where the authors used light pulses to generate and dynamically control electron vortex beams. They showed that when femtosecond electron pulses interact with chiral plasmons that possess OAM, the electron's wavefunction takes on vortex modulation due to energy-momentum conservation. The OAM chiral plasmons are created when light is incident on a nanoscale cavity on a Ag/Si_3N_4 interface. Varying the delay time between electron pulses can result in a coherent modulation of the intensity, periodicity and helicity of the plasmon fringes produced.

Bibliography

[1] Chuanwu Cao and Jian-Hao Chen. Quantum spin hall materials. *Advanced Quantum Technologies*, 2(10):1900026, 2019.

[2] JE Hirsch. Spin hall effect. *Physical review letters*, 83(9):1834, 1999.

[3] Xiaohui Ling, Xinxing Zhou, Kun Huang, Yachao Liu, Cheng-Wei Qiu, Hailu Luo, and Shuangchun Wen. Recent advances in the spin hall effect of light. *Reports on Progress in Physics*, 80(6):066401, 2017.

[4] SA Wolf, DD Awschalom, RA Buhrman, JM Daughton, von S von Molnár, ML Roukes, A Yu Chtchelkanova, and DM Treger. Spintronics: a spin-based electronics vision for the future. *science*, 294(5546):1488–1495, 2001.

[5] Liang Fu, Charles L Kane, and Eugene J Mele. Topological insulators in three dimensions. *Physical review letters*, 98(10):106803, 2007.

[6] M Zahid Hasan and Charles L Kane. Colloquium: topological insulators. *Reviews of modern physics*, 82(4):3045, 2010.

[7] David Hsieh, Dong Qian, Lewis Wray, Yiman Xia, Yew San Hor, Robert Joseph Cava, and M Zahid Hasan. A topological dirac insulator in a quantum spin hall phase. *Nature*, 452(7190):970–974, 2008.

[8] YL Chen, James G Analytis, J-H Chu, ZK Liu, S-K Mo, Xiao-Liang Qi, HJ Zhang, DH Lu, Xi Dai, Zhong Fang, et al. Experimental realization of a three-dimensional topological insulator, bi2te3. *science*, 325(5937):178–181, 2009.

[9] Konstantin Y Bliokh, Daria Smirnova, and Franco Nori. Quantum spin hall effect of light. *Science*, 348(6242):1448–1451, 2015.

[10] Todd Van Mechelen and Zubin Jacob. Universal spin-momentum locking of evanescent waves. *Optica*, 3(2):118–126, 2016.

[11] RJ Coles, DM Price, JE Dixon, B Royall, E Clarke, P Kok, MS Skolnick, AM Fox, and MN Makhonin. Chirality of nanophotonic waveguide with embedded quantum emitter for unidirectional spin transfer. *Nature communications*, 7(1):1–7, 2016.

[12] Konstantin Y Bliokh, Aleksandr Y Bekshaev, and Franco Nori. Extraordinary momentum and spin in evanescent waves. *Nature communications*, 5(1):1–8, 2014.

[13] Konstantin Y Bliokh and Franco Nori. Transverse spin of a surface polariton. *Physical review A*, 85(6):061801, 2012.

[14] Konstantin Yu Bliokh, Francisco J Rodríguez-Fortuño, Franco Nori, and Anatoly V Zayats. Spin–orbit interactions of light. *Nature Photonics*, 9(12):796–808, 2015.

[15] Konstantin Y Bliokh and Franco Nori. Transverse and longitudinal angular momenta of light. *Physics Reports*, 592:1–38, 2015.

[16] Y Yermakov, Anton I Ovcharenko, Andrey A Bogdanov, Ivan V Iorsh, Konstantin Y Bliokh, and Yuri S Kivshar. Spin control of light with hyperbolic metasurfaces. *Physical Review B*, 94(7):075446, 2016.

[17] Daniel O'connor, Pavel Ginzburg, Francisco J Rodríguez-Fortuño, Greg A Wurtz, and Anatoly V Zayats. Spin–orbit coupling in surface plasmon scattering by nanostructures. *Nature communications*, 5(1):1–7, 2014.

[18] Sara M Kandil and Daniel F Sievenpiper. C-shaped chiral waveguide for spin-dependent unidirectional propagation. *Applied Physics Letters*, 118(10):101104, 2021.

[19] J Bisharat Dia'aaldin and Daniel F Sievenpiper. Guiding waves along an infinitesimal line between impedance surfaces. *Physical review letters*, 119(10):106802, 2017.

[20] Jiao Lin, JP Balthasar Mueller, Qian Wang, Guanghui Yuan, Nicholas Antoniou, Xiao-Cong Yuan, and Federico Capasso. Polarization-controlled tunable directional coupling of surface plasmon polaritons. *Science*, 340(6130):331–334, 2013.

[21] Yarden Mazor and Andrea Alù. Routing optical spin and pseudospin with metasurfaces. *Physical Review Applied*, 14(1):014029, 2020.

[22] Lingling Huang, Xianzhong Chen, Benfeng Bai, Qiaofeng Tan, Guofan Jin, Thomas Zentgraf, and Shuang Zhang. Helicity dependent directional surface plasmon polariton excitation using a metasurface with interfacial phase discontinuity. *Light: Science & Applications*, 2(3):e70–e70, 2013.

[23] Francisco J Rodríguez-Fortuño, Giuseppe Marino, Pavel Ginzburg, Daniel O'Connor, Alejandro Martínez, Gregory A Wurtz, and Anatoly V Zayats. Near-field interference for the unidirectional excitation of electromagnetic guided modes. *Science*, 340(6130):328–330, 2013.

[24] Xiaobo Yin, Ziliang Ye, Junsuk Rho, Yuan Wang, and Xiang Zhang. Photonic spin hall effect at metasurfaces. *Science*, 339(6126):1405–1407, 2013.

[25] Nir Shitrit, Igor Yulevich, Elhanan Maguid, Dror Ozeri, Dekel Veksler, Vladimir Kleiner, and Erez Hasman. Spin-optical metamaterial route to spin-controlled photonics. *Science*, 340(6133):724–726, 2013.

[26] Jan Petersen, Jürgen Volz, and Arno Rauschenbeutel. Chiral nanophotonic waveguide interface based on spin-orbit interaction of light. *Science*, 346(6205):67–71, 2014.

[27] Onur Hosten and Paul Kwiat. Observation of the spin hall effect of light via weak measurements. *Science*, 319(5864):787–790, 2008.

[28] Xiaohui Ling, Xinxing Zhou, Xunong Yi, Weixing Shu, Yachao Liu, Shizhen Chen, Hailu Luo, Shuangchun Wen, and Dianyuan Fan. Giant photonic spin hall effect in momentum space in a structured metamaterial with spatially varying birefringence. *Light: Science & Applications*, 4(5):e290–e290, 2015.

[29] Polina V Kapitanova, Pavel Ginzburg, Francisco J Rodríguez-Fortuño, Dmitry S Filonov, Pavel M Voroshilov, Pavel A Belov, Alexander N Poddubny, Yuri S Kivshar, Gregory A Wurtz, and Anatoly V Zayats. Photonic spin hall effect in hyperbolic metamaterials for polarization-controlled routing of subwavelength modes. *Nature communications*, 5(1):1–8, 2014.

[30] Wensheng Ruan, Xintao He, Fuli Zhao, and Jian-Wen Dong. Analysis of unidirectional coupling in topological valley photonic crystal waveguides. *Journal of Lightwave Technology*, 2020.

[31] Dia'aaldin J Bisharat and Daniel F Sievenpiper. Electromagnetic-dual metasurfaces for topological states along a 1d interface. *Laser & Photonics Reviews*, 13(10):1900126, 2019.

[32] Yuting Yang, Yun Fei Xu, Tao Xu, Hai-Xiao Wang, Jian-Hua Jiang, Xiao Hu, and Zhi Hong Hang. Visualization of a unidirectional electromagnetic waveguide using topological photonic crystals made of dielectric materials. *Physical review letters*, 120(21):217401, 2018.

[33] Michela F Picardi, Alejandro Manjavacas, Anatoly V Zayats, and Francisco J Rodríguez-Fortuño. Unidirectional evanescent-wave coupling from circularly polarized electric and magnetic dipoles: An angular spectrum approach. *Physical Review B*, 95(24):245416, 2017.

[34] Michela F Picardi, Anatoly V Zayats, and Francisco J Rodríguez-Fortuño. Janus and huygens dipoles: Near-field directionality beyond spin-momentum locking. *Physical review letters*, 120(11):117402, 2018.

[35] Alba Espinosa-Soria and Alejandro Martinez. Transverse spin and spin-orbit coupling in silicon waveguides. *IEEE Photonics Technology Letters*, 28(14):1561–1564, 2016.

[36] John R Schaibley, Hongyi Yu, Genevieve Clark, Pasqual Rivera, Jason S Ross, Kyle L Seyler, Wang Yao, and Xiaodong Xu. Valleytronics in 2d materials. *Nature Reviews Materials*, 1(11):1–15, 2016.

[37] Gwanho Yoon, Dasol Lee, Ki Tae Nam, and Junsuk Rho. Geometric metasurface enabling polarization independent beam splitting. *Scientific reports*, 8(1):1–8, 2018.

[38] Yannick Lefier and Thierry Grosjean. Unidirectional sub-diffraction waveguiding based on optical spin–orbit coupling in subwavelength plasmonic waveguides. *Optics letters*, 40(12):2890–2893, 2015.

[39] Shuai Zu, Tianyang Han, Meiling Jiang, Feng Lin, Xing Zhu, and Zheyu Fang. Deep-subwavelength resolving and manipulating of hidden chirality in achiral nanostructures. *ACS nano*, 12(4):3908–3916, 2018.

[40] Dries Vercruysse, Yannick Sonnefraud, Niels Verellen, Fabian B Fuchs, Giuliana Di Martino, Liesbet Lagae, Victor V Moshchalkov, Stefan A Maier, and Pol Van Dorpe. Unidirectional side scattering of light by a single-element nanoantenna. *Nano letters*, 13(8):3843–3849, 2013.

[41] Feng Lu, Jongwon Lee, Aiting Jiang, Seungyong Jung, and Mikhail A Belkin. Thermopile detector of light ellipticity. *Nature communications*, 7(1):1–6, 2016.

[42] Atefeh Fazel Najafabadi and Tavakol Pakizeh. Analytical chiroptics of 2d and 3d nanoantennas. *ACS photonics*, 4(6):1447–1452, 2017.

[43] Lauren A McCarthy, Kyle W Smith, Xiang Lan, Seyyed Ali Hosseini Jebeli, Luca Bursi, Alessandro Alabastri, Wei-Shun Chang, Peter Nordlander, and Stephan Link. Polarized evanescent waves reveal trochoidal dichroism. *Proceedings of the National Academy of Sciences*, 117(28):16143–16148, 2020.

[44] Sergey S Kruk, Manuel Decker, Isabelle Staude, Stefan Schlecht, Michael Greppmair, Dragomir N Neshev, and Yuri S Kivshar. Spin-polarized photon emission by resonant multipolar nanoantennas. *ACS Photonics*, 1(11):1218–1223, 2014.

[45] Weimin Ye, Franziska Zeuner, Xin Li, Bernhard Reineke, Shan He, Cheng-Wei Qiu, Juan Liu, Yongtian Wang, Shuang Zhang, and Thomas Zentgraf. Spin and wavelength multiplexed nonlinear metasurface holography. *Nature communications*, 7(1):1–7, 2016.

[46] Francisco J Rodríguez-Fortuño, Daniel Puerto, Amadeu Griol, Laurent Bellieres, Javier Martí, and Alejandro Martínez. Sorting linearly polarized photons with a single scatterer. *Optics letters*, 39(6):1394–1397, 2014.

[47] Francisco J Rodríguez-Fortuño, Isaac Barber-Sanz, Daniel Puerto, Amadeu Griol, and Alejandro Martínez. Resolving light handedness with an on-chip silicon microdisk. *ACS Photonics*, 1(9):762–767, 2014.

[48] S Bassiri, CH Papas, and Nader Engheta. Electromagnetic wave propagation through a dielectric–chiral interface and through a chiral slab. *JOSA A*, 5(9):1450–1459, 1988.

[49] Jungho Mun, Minkyung Kim, Younghwan Yang, Trevon Badloe, Jincheng Ni, Yang Chen, Cheng-Wei Qiu, and Junsuk Rho. Electromagnetic chirality: from fundamentals to nontraditional chiroptical phenomena. *Light: Science & Applications*, 9(1):1–18, 2020.

[50] E Plum, VA Fedotov, and NI Zheludev. Optical activity in extrinsically chiral metamaterial. *Applied physics letters*, 93(19):191911, 2008.

[51] Na Liu and Harald Giessen. Coupling effects in optical metamaterials. *Angewandte Chemie International Edition*, 49(51):9838–9852, 2010.

[52] Xin-Tao He, En-Tao Liang, Jia-Jun Yuan, Hao-Yang Qiu, Xiao-Dong Chen, Fu-Li Zhao, and Jian-Wen Dong. A silicon-on-insulator slab for topological valley transport. *Nature communications*, 10(1):1–9, 2019.

[53] Hou-Tong Chen, Antoinette J Taylor, and Nanfang Yu. A review of metasurfaces: physics and applications. *Reports on progress in physics*, 79(7):076401, 2016.

[54] Aobo Li, Shreya Singh, and Dan Sievenpiper. Metasurfaces and their applications. *Nanophotonics*, 7(6):989–1011, 2018.

[55] Ryan Quarfoth and Daniel Sievenpiper. Artificial tensor impedance surface waveguides. *IEEE transactions on antennas and propagation*, 61(7):3597–3606, 2013.

[56] Jiyeon Lee and Daniel F Sievenpiper. Patterning technique for generating arbitrary anisotropic impedance surfaces. *IEEE Transactions on Antennas and Propagation*, 64(11):4725–4732, 2016.

[57] Sergei A Kuznetsov, Mikhail A Astafev, Miguel Beruete, and Miguel Navarro-Cía. Planar holographic metasurfaces for terahertz focusing. *Scientific reports*, 5(1):1–8, 2015.

[58] Fei Ding, Yiting Chen, and Sergey I Bozhevolnyi. Focused vortex-beam generation using gap-surface plasmon metasurfaces. *Nanophotonics*, 9(2):371–378, 2020.

[59] Fei Ding, Yiting Chen, and Sergey I Bozhevolnyi. Gap-surface plasmon metasurfaces for linear-polarization conversion, focusing, and beam splitting. *Photonics Research*, 8(5):707–714, 2020.

[60] Xueyu Chen, Haijian Zou, Mingyang Su, Linwei Tang, Chaofeng Wang, Shuqing Chen, Chenliang Su, and Ying Li. All-dielectric metasurface-based beam splitter with arbitrary splitting ratio. *Nanomaterials*, 11(5):1137, 2021.

[61] Yihao Yang, Liqiao Jing, Lian Shen, Zuojia Wang, Bin Zheng, Huaping Wang, Erping Li, Nian-Hai Shen, Thomas Koschny, Costas M Soukoulis, et al. Hyperbolic spoof plasmonic metasurfaces. *NPG Asia Materials*, 9(8):e428–e428, 2017.

[62] Daniel F Sievenpiper. Forward and backward leaky wave radiation with large effective aperture from an electronically tunable textured surface. *IEEE transactions on antennas and propagation*, 53(1):236–247, 2005.

[63] Wenwei Liu, Hua Cheng, Jianguo Tian, and Shuqi Chen. Diffractive metalens: from fundamentals, practical applications to current trends. *Advances in Physics: X*, 5(1):1742584, 2020.

[64] Dennis W Prather, Shouyuan Shi, Janusz Murakowski, Garrett J Schneider, Ahmed Sharkawy, Caihua Chen, BingLin Miao, and Richard Martin. Self-collimation in photonic crystal structures: a new paradigm for applications and device development. *Journal of Physics D: Applied Physics*, 40(9):2635, 2007.

[65] Yi-Chen Chuang. *Complex photonic crystals for broadband "all-angle" self-collimation*. PhD thesis, The University of North Carolina at Charlotte, 2010.

[66] Jeremy Witzens, Marko Loncar, and Axel Scherer. Self-collimation in planar photonic crystals. *IEEE Journal of Selected Topics in Quantum Electronics*, 8(6):1246–1257, 2002.

[67] Ibrahim H Giden, Mirbek Turduev, and Hamza Kurt. Broadband super-collimation with low-symmetric photonic crystal. *Photonics and Nanostructures-Fundamentals and Applications*, 11(2):132–138, 2013.

[68] Dingshan Gao, Zhiping Zhou, and David S Citrin. Self-collimated waveguide bends and partial bandgap reflection of photonic crystals with parallelogram lattice. *JOSA A*, 25(3):791–795, 2008.

[69] Yi Xu, Xiao-Jun Chen, Sheng Lan, Qi Guo, Wei Hu, and Li-Jun Wu. The all-angle self-collimating phenomenon in photonic crystals with rectangular symmetry. *Journal of Optics A: Pure and Applied Optics*, 10(8):085201, 2008.

[70] Sara M Kandil, Dia'aaldin J Bisharat, and Daniel F Sievenpiper. Chiral surface wave propagation with anomalous spin-momentum locking. *ACS Photonics*.

[71] Nasim Mohammadi Estakhri and Andrea Alù. Recent progress in gradient metasurfaces. *JOSA B*, 33(2):A21–A30, 2016.

[72] Nanfang Yu, Patrice Genevet, Mikhail A Kats, Francesco Aieta, Jean-Philippe Tetienne, Federico Capasso, and Zeno Gaburro. Light propagation with phase discontinuities: generalized laws of reflection and refraction. *science*, 334(6054):333–337, 2011.

[73] Carl Pfeiffer and Anthony Grbic. Metamaterial huygens' surfaces: tailoring wave fronts with reflectionless sheets. *Physical review letters*, 110(19):197401, 2013.

[74] Michael V Berry. The adiabatic phase and pancharatnam's phase for polarized light. *Journal of Modern Optics*, 34(11):1401–1407, 1987.

[75] Huanhuan Yang, Xiangyu Cao, Fan Yang, Jun Gao, Shenheng Xu, Maokun Li, Xibi Chen, Yi Zhao, Yuejun Zheng, and Sijia Li. A programmable metasurface with dynamic polarization, scattering and focusing control. *Scientific reports*, 6(1):1–11, 2016.

[76] Christophe Caloz and Ari Sihvola. Electromagnetic chirality, part 1: the microscopic perspective [electromagnetic perspectives]. *IEEE Antennas and Propagation Magazine*, 62(1):58–71, 2020.

[77] Karim Achouri and Olivier JF Martin. Fundamental properties and classification of polarization converting bianisotropic metasurfaces. *IEEE Transactions on Antennas and Propagation*, 69(9):5653–5663, 2021.

[78] Viktar S Asadchy and Sergei A Tretyakov. Modular analysis of arbitrary dipolar scatterers. *Physical Review Applied*, 12(2):024059, 2019.

[79] Yachao Liu, Xiaohui Ling, Xunong Yi, Xinxing Zhou, Shizhen Chen, Yougang Ke, Hailu Luo, and Shuangchun Wen. Photonic spin hall effect in dielectric metasurfaces with rotational symmetry breaking. *Optics letters*, 40(5):756–759, 2015.

[80] Konstantin Y Bliokh, Yuri Gorodetski, Vladimir Kleiner, and Erez Hasman. Coriolis effect in optics: unified geometric phase and spin-hall effect. *Physical review letters*, 101(3):030404, 2008.

[81] Hamza Kurt, M Turduev, and IH Giden. Crescent shaped dielectric periodic structure for light manipulation. *Optics express*, 20(7):7184–7194, 2012.

[82] Gene Dresselhaus. Spin-orbit coupling effects in zinc blende structures. *Physical Review*, 100(2):580, 1955.

[83] EIJSP Rashba. Properties of semiconductors with an extremum loop. i. cyclotron and combinational resonance in a magnetic field perpendicular to the plane of the loop. *Sov. Phys.-Solid State*, 2:1109, 1960.

[84] John Price Hirth, Jens Lothe, and T Mura. Theory of dislocations. *Journal of Applied Mechanics*, 50(2):476, 1983.

[85] Nils G Weimann, Lester F Eastman, Dharanipal Doppalapudi, Hock M Ng, and Theodore D Moustakas. Scattering of electrons at threading dislocations in gan. *Journal of Applied Physics*, 83(7):3656–3659, 1998.

[86] David C Look and JR Sizelove. Dislocation scattering in gan. *Physical review letters*, 82(6):1237, 1999.

[87] HM Ng, D Doppalapudi, TD Moustakas, NG Weimann, and LF Eastman. The role of dislocation scattering in n-type gan films. *Applied physics letters*, 73(6):821–823, 1998.

[88] Ying Ran, Yi Zhang, and Ashvin Vishwanath. One-dimensional topologically protected modes in topological insulators with lattice dislocations. *Nature Physics*, 5(4):298–303, 2009.

[89] Xiaoyin Li, Shunhong Zhang, Huaqing Huang, Lin Hu, Feng Liu, and Qian Wang. Unidirectional spin–orbit interaction induced by the line defect in monolayer transition metal dichalcogenides for high-performance devices. *Nano Letters*, 19(9):6005–6012, 2019.

[90] Lin Hu, Huaqing Huang, Zhengfei Wang, Wei Jiang, Xiaojuan Ni, Yinong Zhou, V Zielasek, MG Lagally, Bing Huang, and Feng Liu. Ubiquitous spin-orbit coupling in a screw dislocation with high spin coherency. *Physical review letters*, 121(6):066401, 2018.

[91] Moh Adhib Ulil Absor, Iman Santoso, Naoya Yamaguchi, and Fumiyuki Ishii. Spin splitting with persistent spin textures induced by the line defect in the 1 t phase of monolayer transition metal dichalcogenides. *Physical Review B*, 101(15):155410, 2020.

[92] Haoran Xue, Ding Jia, Yong Ge, Yi-jun Guan, Qiang Wang, Shou-qi Yuan, Hong-xiang Sun, YD Chong, and Baile Zhang. Observation of dislocation-induced topological modes in a three-dimensional acoustic topological insulator. *Physical Review Letters*, 127(21):214301, 2021.

[93] Qian Lin, Xiao-Qi Sun, Meng Xiao, Shou-Cheng Zhang, and Shanhui Fan. A three-dimensional photonic topological insulator using a two-dimensional ring resonator lattice with a synthetic frequency dimension. *Science advances*, 4(10):eaat2774, 2018.

[94] Ling Lu, Haozhe Gao, and Zhong Wang. Topological one-way fiber of second chern number. *Nature communications*, 9(1):1–7, 2018.

[95] Robert D Meade, Joshua N Winn, and J Joannopoulos. Photonic crystals: Molding the flow of light. *Pinceton Univ. Press*, 1995.

[96] KM Ho, Che Ting Chan, and Costas M Soukoulis. Existence of a photonic gap in periodic dielectric structures. *Physical Review Letters*, 65(25):3152, 1990.

[97] Siyuan Luo, Li He, and Mo Li. Spin-momentum locked interaction between guided photons and surface electrons in topological insulators. *Nature communications*, 8(1):1–7, 2017.

[98] Giovanni Maria Vanacore, Gabriele Berruto, Ivan Madan, Enrico Pomarico, P Biagioni, RJ Lamb, D McGrouther, O Reinhardt, I Kaminer, B Barwick, et al. Ultrafast generation and control of an electron vortex beam via chiral plasmonic near fields. *Nature materials*, 18(6):573–579, 2019.